

Article

Strength-Toughness Balance and Hydrogen Embrittlement Susceptibility of a Precipitation-Strengthened Steel Adopted Tempering Process

Ning Zhao ¹, Yanlin He ^{1,*}, Li Lin ², Rendong Liu ², Qiangqiang Zhao ¹ and Weisen Zheng ¹

¹ State Key Laboratory of Advanced Special Steel, School of Materials Science and Engineering, Shanghai University, Shanghai 200444, China

² Ansteel Group Co., Ltd., Anshan 114021, China

* Correspondence: ylhe@t.shu.edu.cn; Tel.: +86-021-5633-1472

Abstract: Two steels with different Nickel (Ni) content were investigated to reveal the role of Ni on strength-toughness balance and hydrogen embrittlement susceptibility. Although they were similar in microstructure, i.e., nano-particles were precipitated on martensitic laths, different mechanical behaviors were exhibited. After tempering, the yield strength of 3.5 Ni steel reached a peak at 500 °C, while that of 2.5 Ni steel kept a downward trend, indicating that precipitation strengthening was significant in 3.5 Ni steel. Combined with thermodynamic and kinetic analyses, it was shown that when the Ni content increased, the rich-copper (Cu) precipitation transformation driving force would be enhanced and the reverse of austenite transformation accelerated to improve its stability. Moreover, the increase of Ni content also induced the increase in high-angle grain boundaries (HAGBs), which could inhibit crack propagation. Under the comprehensive effects of strengthening and ductility mechanism, 3.5 Ni steel exhibited excellent cryogenic toughness. Although it was not possible to obtain the ideal balancing of strength-toughness for the steel with lower Ni content, its hydrogen embrittlement susceptibility is satisfying. The results showed that the increase of grain boundary density caused by the grain refinement of 2.5 Ni steel is the key factor for its lower hydrogen embrittlement sensitivity index. Moreover, with the reduction of Ni content, the decrease of HAGBs and the increase in $\Sigma 11$ boundary were conducive to reducing hydrogen-assisted cracking, while the residual Fe₃C in 3.5 Ni steel would deteriorate the hydrogen embrittlement resistance.

Keywords: nickel element; strength-toughness balance; grain boundaries; hydrogen embrittlement susceptibility



Citation: Zhao, N.; He, Y.; Lin, L.; Liu, R.; Zhao, Q.; Zheng, W. Strength-Toughness Balance and Hydrogen Embrittlement Susceptibility of a Precipitation-Strengthened Steel Adopted Tempering Process. *Metals* **2022**, *12*, 1534. <https://doi.org/10.3390/met12091534>

Academic Editors: Zhenjia Xie, Xueda Li and Xiangliang Wan

Received: 10 August 2022

Accepted: 13 September 2022

Published: 16 September 2022

Publisher's Note: MDPI stays neutral with regard to jurisdictional claims in published maps and institutional affiliations.



Copyright: © 2022 by the authors. Licensee MDPI, Basel, Switzerland. This article is an open access article distributed under the terms and conditions of the Creative Commons Attribution (CC BY) license (<https://creativecommons.org/licenses/by/4.0/>).

1. Introduction

Low-carbon steel with ultrahigh strength and satisfactory cryogenic toughness is the cost-efficient material solution for the lightweight structural design strategy of offshore engineering. The strengthening effects of Cu precipitation on the steels have been well documented [1]. However, the addition of Cu will cause hot shortness during the hot rolling process [2]. Thus, Cu-strengthened steels are characterized by high Ni content. Meanwhile, the increase of Ni content can reduce the ductile-brittle transition temperature (DBTT) and improve transgranular cleavage resistance [3]. High Ni-alloyed steel, such as 9 Ni steel, has been widely used as the main material for low-temperature material storage because of its excellent cryogenic toughness [4]. By quenching and tempering process (QT), thermally stable austenite can be formed at the boundary of the martensitic matrix for 9 Ni steel, which can prevent crack propagation in a harsh environment. In contrast, for steel with lower Ni content, such as 5 Ni steels, the reduction of Ni content reduces the austenite content in the steel and weakens the toughness of the steel [5]. To maintain excellent cryogenic toughness of steel with lower Ni content, many works [6,7] applied the quenching-intercritical annealing-tempering (QLT) process to obtain stable

austenite. However, compared with the traditional QT process, the QLT process will reduce the strength of steel, and it is difficult for its yield strength to exceed 1000 MPa. Moreover, with same effect as the higher Ni content, the complexity of the process can also increase the production cost. In our recent work, the steels with about 3 wt.% Ni content were developed adopting the QT process, and have exhibited the yield strength above 1030 MPa at room temperature and the impact energy above 69 J at $-40\text{ }^{\circ}\text{C}$, whose performance can almost compare favorably with 9 Ni steel [8]. The development of low Ni steel with excellent properties is feasible, and further investigation of the strengthening and toughening mechanism of low Ni steel is significant for the development of novel high-performance steel.

Besides meeting the strength and cryogenic toughness, offshore steel faces another challenge, i.e., hydrogen embrittlement, during service in practical environments. Especially when the tensile strength of the steel exceeds $\sim 1\text{ GPa}$, the mechanical properties of the steel are degraded due to hydrogen embrittlement, which may lead to delayed or sudden failure [9]. As well known, the hydrogen embrittlement susceptibility is mainly dependent on the diffusible hydrogen atoms in steel, which are related to microstructure, second phases and dislocations, etc., [10]. Generally, optimizing alloy composition and regulating the microstructure can be used to effectively alleviate the hydrogen embrittlement of high-strength steel. For example, the addition of microalloying elements Nb is an effective method for improving the hydrogen embrittlement resistance of high strength steel mainly through the hydrogen trapping mechanism [11]. As an alloying element widely used in structural steel, the effect of Ni on the hydrogen embrittlement resistance of high-strength structural steel has still been obscure. Cunha et al. [12] found that 9 Ni steel tempered at $600\text{ }^{\circ}\text{C}$ was less sensitive to sulfide stress corrosion cracking (SSCC) because of the hydrogen trap effect of austenite. When the hydrogen embrittlement behavior of high-strength steel with about 1 wt.% Ni content was investigated, Hui et al. [13] also concluded that the addition of Ni could further decrease the hydrogen embrittlement susceptibility, owing to enhanced corrosion resistance and decreased hydrogen absorption. However, Park et al. [14] recently pointed out that with the increase of Ni content from 0.3 wt.% to 1.2 wt.%, the hydrogen embrittlement susceptibility of experimental steel first decreased and then increased, which resulted from a higher fraction of undissolved Fe_3C in austenitized steel with higher Ni content. Therefore, it is necessary to elucidate the hydrogen embrittlement mechanism responding to the complex microstructure evolution.

In the present work, the mechanical performance of two low carbon steels with different Ni contents adopting quenching and tempering were emphasized, and the microstructure evolution was discussed based on nucleation and diffusion theories. Moreover, the hydrogen embrittlement resistance of the two steels was also evaluated by comparing the tensile properties before and after hydrogen charging. Combined with the microstructure characteristics, the effect of Ni content on the mechanical properties and hydrogen embrittlement susceptibility of the steel was further elucidated.

2. Experimental

2.1. Materials and Heat Treatments

20 kg ingots with the chemical composition shown in Table 1 were melted in a vacuum induction furnace and cast in the laboratory. The amount of Ni in steels was designed to be 2.5 and 3.5 wt.%, which were designated as 2.5 Ni and 3.5 Ni steel, respectively. To pursue better weldability, the carbon (C) content was designed below 0.1 wt.%. Slabs of 40 mm thickness were cut from the ingot by using wire-electrode cutting machine, then homogenized at $1150\text{ }^{\circ}\text{C}$ for 1 h and then hot rolled into 14 mm thickness plates by several passes. The heat-treated specimens with dimensions of $11 \times 14 \times 100\text{ mm}^3$ and $12 \times 14 \times 60\text{ mm}^3$ were cut from the rolled steel plate. After heat treatment, they were used to process the tensile samples and Charpy impact samples, respectively. The temperature of heat treatment was based on phase transformation temperature. Dilatometric measurement was carried out in a DIL805A dilatometer (BÄHR-Thermoanalyse GmbH Ltd., Hüllhorst,

Germany) using cylindrical specimens of 4 mm in diameter and 10 mm in length. As shown in Figure 1, the austenitizing temperatures (A_{c3}) of both steels were determined to be 828.5 and 814.5 °C, respectively. Accordingly, the samples were solution treated at 860 °C for 25 min, followed by water-quenching to room temperature noted as Q860. The samples were then tempered at 460, 500, 540, 580 and 620 °C for 35 min followed by air cooling, noted as T460, T500, T540, T580 and T620, respectively.

Table 1. Composition of the two investigated steels (wt.%).

Steels	C	Si	Mn	Cu	Ni	Cr	Mo	Nb
2.5 Ni	0.09	0.07	0.84	1.00	2.5	0.40	0.53	0.05
3.5 Ni	0.09	0.07	0.87	1.05	3.5	0.40	0.56	0.05

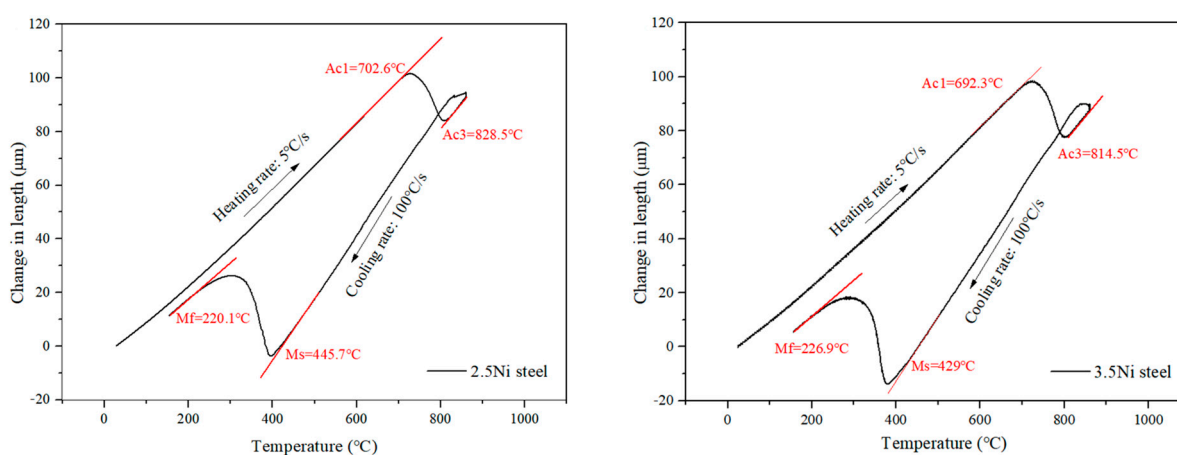


Figure 1. Dilatometric curve of the hot-rolled specimen for both steels.

2.2. Mechanical Tests and Fracture Analysis

Tensile samples with a diameter of 5 mm and a gauge length of 25 mm were wire-cut and conducted on the MTS Alliance RT 30 tensile testing machine with a strain rate of 0.001/s (1.5 mm/min) at room temperature. Impact tests were performed at -40 °C according to the standard GB/T 229. The strength and toughness values presented here were an average of three measurements. The fracture surfaces were observed using scanning electron microscopy (SEM, Sigma 300, Zeiss, Jena, Germany).

2.3. Microstructure Observation

After being mechanically grounded and polished, quenched samples were etched with supersaturated picric acid and characterized by optical microscopy (OM) to measure the prior austenite grain (PAG) size using the linear intercept method. The microstructure morphologies of the samples were etched with 4% Nital solution and characterized by SEM. Further electron backscatter diffraction (EBSD) technique was exploited to reveal the crystallographic characteristics. EBSD samples were electro-polished in 10% perchloric acid alcohol solution and observed with a step size of 0.08 μm . To identify the constituent phases and estimate the dislocation densities by the modified Williamson-Hall method [15], X-ray diffraction (XRD) analyses were performed on a 3 KW D/MAX2200V (Rigaku Corp., Tokyo, Japan) diffractometer. Data collection was conducted by using Cu K α radiation in the 2θ range of 40–100° and with a scan step interval of 2°/min. Transmission electron microscope (TEM) observations were carried out on a JEOL 2100F (JEOL Ltd., Tokyo, Japan) instrument equipped with energy dispersive spectroscopy (EDS), operated at 200 kV. The 60 μm TEM foils were further thinned in 10% perchloric acid alcohol by twin-jet electropolishing at 35 V and -30 °C. Also, the carbon extraction replica technique was used to investigate the morphology and size of nano-particles. Thermodynamic and kinetic analyses were

carried out using Thermo-Calc (TC) (Version 2020a. Royal Institute of Technology (KTH), Stockholm, Sweden) and DICTRA (Version 2020a. Royal Institute of Technology (KTH), Stockholm, Sweden) with TCFE10 and MOBFE5 databases.

2.4. Hydrogen Induced Embrittlement and Analysis

To study the effect of hydrogen atoms on the tensile properties of the two steels, hydrogen was electrochemically pre-charged into the tensile samples. Firstly, the sample surface was mechanically grounded to 1200 grit using silicon carbide paper. Then, hydrogen was charged into the entire sample in an aqueous solution of 0.5 mol/L H₂SO₄ containing 0.25 g/L NH₄SCN at 0.5 mA/cm² for 2.5 h. No hydrogen damage was found on the specimen surfaces. After hydrogen charging, the specimens were immediately subjected to the tensile test immediately at the same strain rate as the tensile test (0.001/s). These samples are named “AR-H”. Fractography observation was undertaken using SEM. To quantitatively evaluate hydrogen embrittlement susceptibility, two hydrogen embrittlement indexes were defined as follows:

$$El_{HEI} = \frac{El_{uncharged} - El_{charged}}{El_{uncharged}} \times 100\% \quad (1)$$

$$Ra_{HEI} = \frac{Ra_{uncharged} - Ra_{charged}}{Ra_{uncharged}} \times 100\% \quad (2)$$

where *El* and *Ra* are the total elongation and the reduction in area, respectively. The subscript *HEI*, *uncharged* and *charged* represent the hydrogen embrittlement indexes, the samples without hydrogen charging and the samples with hydrogen charging, respectively. The hydrogen embrittlement susceptibility test of the two steels was repeated three times.

To compare the hydrogen trapping behavior of the two steels, the thermal desorption test was carried out on 2.5 Ni steel using thermal desorption spectrometry (TDS, HTDS-002, R-DEC Co., Ltd., Tsukuba, Japan). The test process is the same as that of 3.5 Ni steel, i.e., the cylinder specimens with 5 mm diameters and 25 mm heights cut from the 2.5 Ni steel were ground to 1200 grit using silicon carbide paper, and hydrogen was introduced into the TDS specimens in an aqueous solution of 0.2 mol/L H₂SO₄ + 0.5g/L NH₄SCN at a current density of 2 mA/cm² for 24 h [11]. In order to meet the requirement of the TDS test, the hydrogen charging condition for TDS are harsher than that for tensile tests. The corresponding hydrogen desorption rate curve was recorded during heating at a constant heating rate of 100 °C/h from room temperature to 800 °C. The hydrogen effusing out of the specimens was analyzed by the quadrupolar mass spectrometer, and the hydrogen content was obtained.

3. Results and Discussion

3.1. Microstructural Evolutions during Heat Treatment Process

Figure 2a,b exhibit the morphologies and size distribution of the PAG of both steels after austenitizing at 860 °C. Statistical results indicate that average PAG sizes of 3.5 Ni and 2.5 Ni steel are 11.73 μm and 10.37 μm, respectively. Moreover, it can be seen that the proportion of grains less than 10 μm in 2.5 Ni steel is more than that in 3.5 Ni steel. It can therefore be concluded that finer grains predominate in 2.5 Ni steel. Because the A_{c3} temperature of 3.5 Ni steel is lower than that of 2.5 Ni steel (Figure 1), under a given austenitizing temperature, the overheating degree of 3.5 Ni steel is large and the grain is easy to coarsen [14]. Figure 2c,d demonstrate a predominantly lath martensitic microstructure for the quenched sample. Due to the larger size of PAG in 3.5 Ni steel, the width and length of martensite lath are larger than those in 2.5 Ni steel. It is worth noting that some particles are observed on the martensitic matrix in sample Q860.

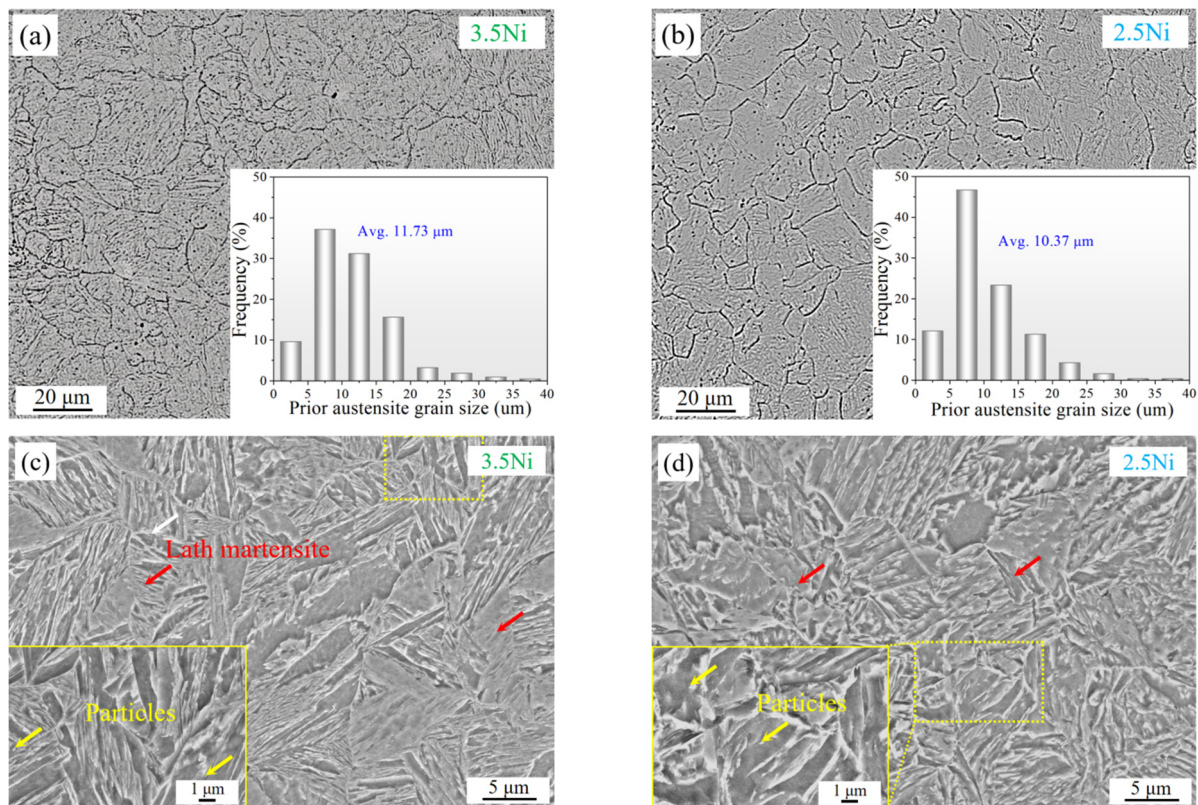


Figure 2. (a,b) OM micrographs of PAG and (c,d) typical SEM micrographs of matrix for the quenched 3.5 Ni and 2.5 Ni steels. Inserted graphs in (a,b) show the distribution curves of the size of PAG.

Figure 3 shows SEM morphologies of experimental steels tempered at 460, 540 and 620 °C. The microstructure is mainly composed of tempered martensite and the carbides at laths boundaries and PAG boundaries (PAGBs, marked with the red dotted line). For 3.5 Ni steel, as the tempering temperature increases from 460 to 620 °C, the martensite lath widens and decomposes, which is ascribed to the strong recovery. Especially, the boundaries of laths with parallel alignment in sample T620 turn “blurred” (Figure 3c) and recrystallization occurs in the local microstructure. The micrographs of 2.5 Ni steel (Figure 3d–f) also show that the recovery degree of martensitic lath increases with the increase of tempering temperature, but its recovery degree is weaker than that of 3.5 Ni steel. As shown by the blue arrow in Figure 3f, parallel martensitic laths are still observed in sample T620 for 2.5 Ni steel. In addition, compared with sample T460, it is found that when tempering at 540 °C, the PAGs are coarsened and the nearby small grains are swallowed up.

In general, the recovery phenomenon involves the reduction of dislocation density. Thus, the dislocation density is estimated by the X-ray diffraction line broadening method. The representative XRD spectra are shown in Figure 4a, which indicates that the matrix of all samples is mainly composed of martensite phase, except for the weak austenite peak detected in sample T500 of 3.5 Ni steel. The result mainly shows four peaks, corresponding to the (110), (200), (211) and (220) crystallographic plane of the bcc structure, respectively. This suggests that when the carbon content is low enough, the diffraction peaks of ferrite and lath martensite are coincident [16]. The dislocation density was calculated using the modified Williamson-Hall (MWH) method based on XRD analysis [15] and shown in Figure 4b. According to the trend of dislocation density, the whole tempering process can be divided into two stages. The first stage occurs in the range of 460–500 °C, in which the dislocation density decreases rapidly and the decline rate of dislocation density of 3.5 Ni steel is faster than that of 2.5 Ni steel. During tempering, the large reduction of dislocation density in martensite is mainly due to the annihilation and recovery process [17]. In the

second stage, the dislocation density increases and then decreases when the tempering temperature increases from 500 °C to 620 °C. This may be related to the transformation of austenite into secondary martensite after tempering. At this time, there is a competitive relationship between the increase of dislocation density caused by the formation of secondary martensite and the decrease of dislocation density caused by the recovery of tempered martensite. The increase of dislocation density is related to the content of austenite in the steel and its stability, which means its ability to transform into secondary martensite when cooled to room temperature.

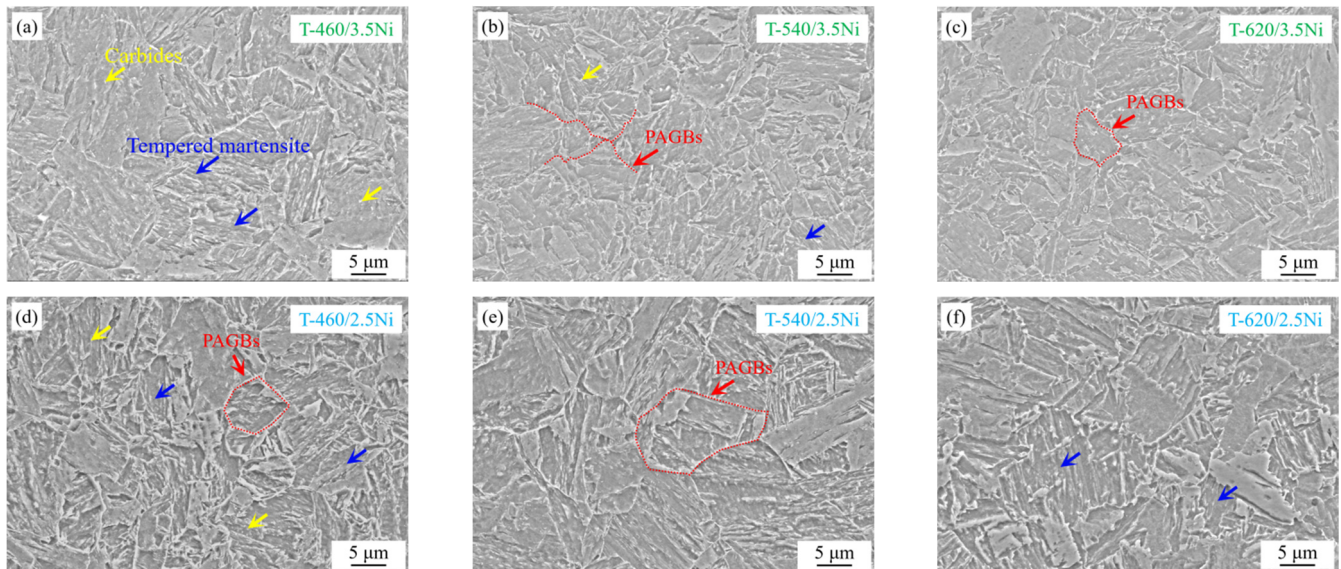


Figure 3. Selected SEM morphologies of both steels after tempering at (a,d) 460, (b,e) 540 and (c,f) 620 °C.

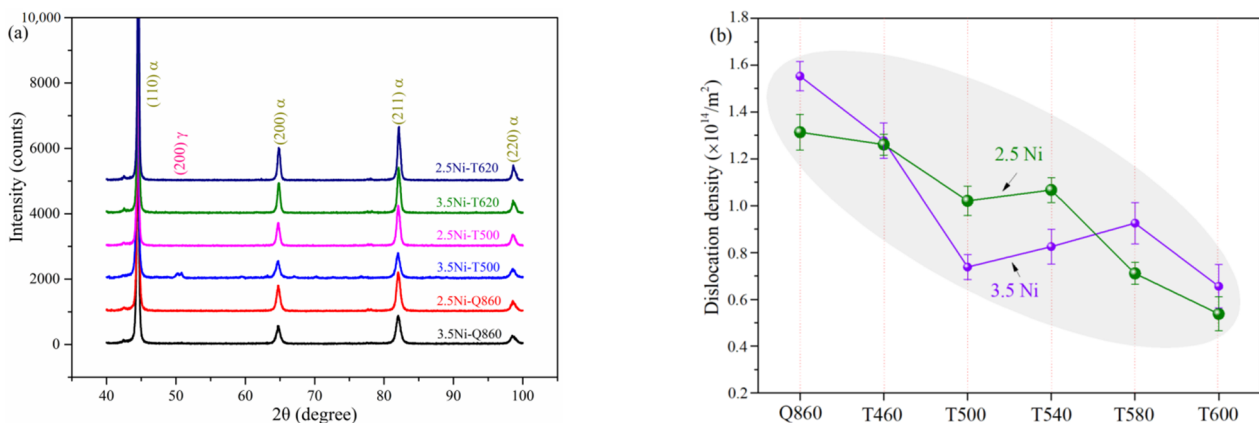


Figure 4. (a) XRD spectra. (b) The relationship between dislocation density and heat treatments process.

TEM characterization and selected area electron diffraction (SAED) of experimental steel under tempering at 500 °C are carried out and presented in Figure 5a,b. The matrix is mainly composed of lath martensite with high-density dislocation. SAED patterns taken from the martensite laths are indexed by following the body-centered tetragonal (bct, α') structure of martensite. As shown in Figure 5c–f, martensite lath and a small amount of thin-film austenite (γ) with a width of about 20 nm can be observed in sample T500 for 3.5 Ni steel, and the orientation relationship between them is $(011)_{\alpha'} // (\bar{1}\bar{1}1)_{\gamma}$, $[11\bar{1}]_{\alpha'} // [011]_{\gamma}$, exhibiting the typical K-S relationship. The presence of austenite is hard to find in sample T500 of 2.5 Ni steel due to its lower content, which is consistent with the XRD results.

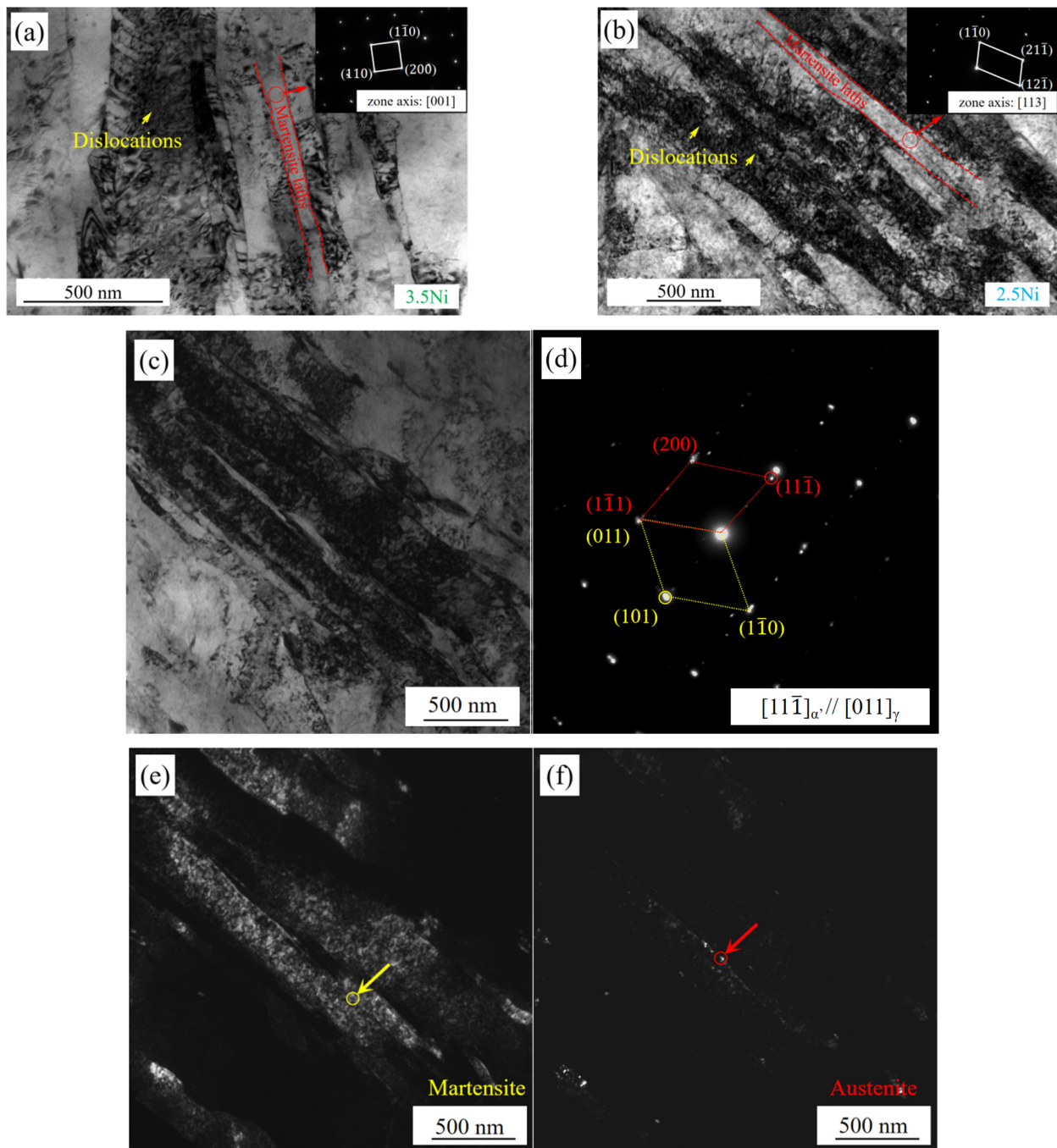


Figure 5. (a,b) TEM micrographs of the typical martensite microstructure of the two steels. (c–f) TEM micrographs of martensite and austenite microstructure in sample T500 of 3.5 Ni steel; (c) bright-field image; (d) SAED pattern; (e) dark field image of martensite with $(101)_{\alpha'}$ reflection; (f) dark field image of austenite with $(111)_{\gamma'}$ reflection.

From the dilatometric curve shown in Figure 1, it can be found that 3.5 Ni steel has a lower M_s temperature, which is conducive to the retention of austenite. However, the retained austenite content in the quenched samples of the two steels is too low to be detected by XRD analysis. After tempering at 500 °C, the austenite peak was observed in XRD results of 3.5 Ni steel, indicating that austenite content increased slightly, which may be related to austenite reverse transformation. Figure 6 shows the austenite evolution during tempering simulated by DICTRA (Version 2020a. Royal Institute of Technology (KTH), Stockholm, Sweden). The schematic diagram of microstructure evolution during tempering is shown

in Figure 6a. Two simulation units, austenite and martensite, were set up, with the initial lath width of 4 nm and 600 nm, respectively. Half of the lath width (2 nm and 300 nm) was used for dynamic calculation. The initial composition was set to be equal to the nominal chemical composition of the steel. It can be seen from Figure 6b that the increase in Ni content accelerates the reverting of austenite, and the effect is more significant with the increase in tempering temperature. The migration distance of interface in 3.5 Ni and 2.5 Ni steels are 33.5 and 25.8 nm after tempering at 620 °C. Figure 6c–f shows the variation of concentration profiles of C and Ni between reverted austenite and martensite in both steels. As shown in Figure 6c,d, the increase of Ni content leads to high Ni segregation at the interface between austenite and martensite, which is conducive to improving the stability of austenite at the interface, and the amount of Ni segregation increases with the increase of tempering temperature. However, the carbon content in austenite will be significantly reduced due to the high diffusion rate of C (Figure 6e,f). Therefore, high tempering temperature will reduce the stability of austenite and the austenite will transform into secondary martensite in the subsequent cooling process. Both experiments and DICTRA simulation show that the content of austenite in 3.5 Ni steel is more than that in 2.5 Ni steel, so more secondary martensite will be formed after high temperature tempering, resulting in an obvious increase in dislocation density in 3.5 Ni steel.

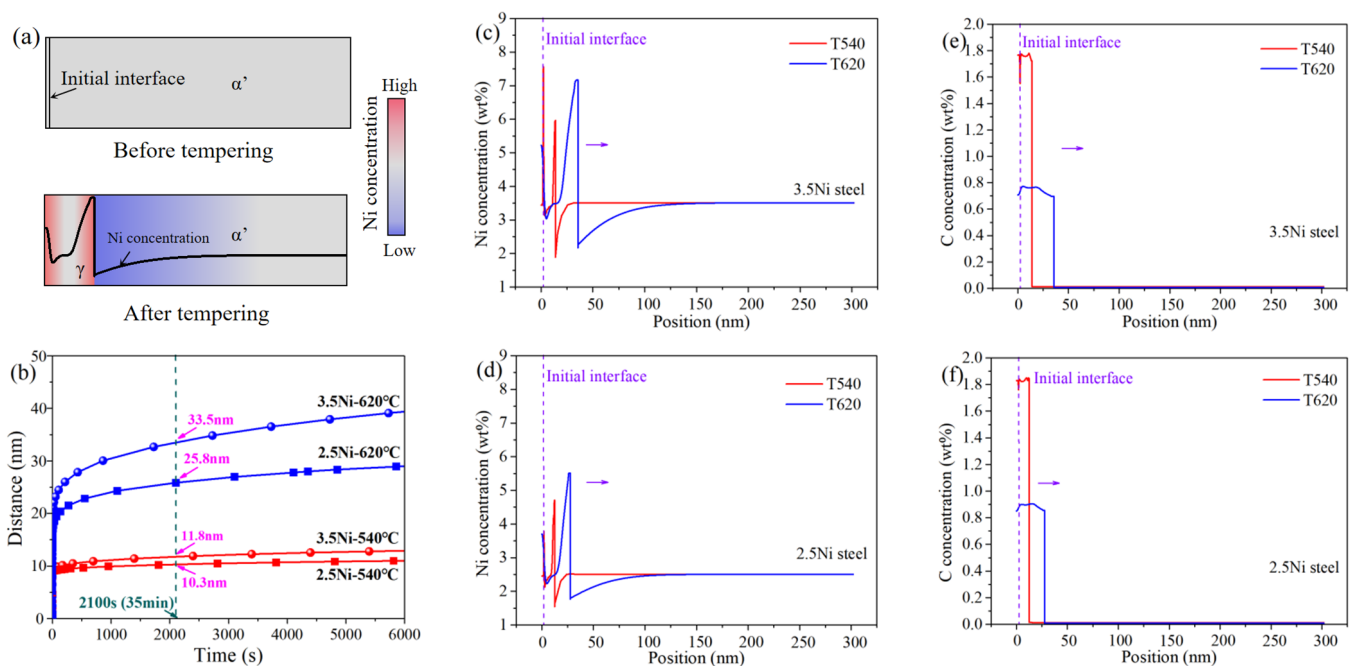


Figure 6. (a) The schematic diagram of movement of austenite/martensite interface during austenite reverted transformation. (b) Relationship between interface moving distance and tempering holding time. (c–f) Variation of concentration profiles of Ni and C with tempering temperature.

Furthermore, a large number of the second phases include $M_{23}C_6$ carbides, rich-Cu precipitates and MC carbides were observed in both steels. Taking 3.5 Ni steel as an example, the second phases were observed and analyzed by TEM (Figures 7–9). As shown in Figure 7a–c, the HAADF-STEM study reveals that martensite lath boundaries in sample T500 are mostly decorated by $M_{23}C_6$ carbide particles. These carbides in the tempered sample have an elongated shape approximately with a length of 120 nm and a width of 10 nm and are present parallel to the martensitic laths. In the STEM images (Figure 7b), the precipitated carbides appear to be brighter in contrast, resulting from very high-angle, incoherently scattered electrons [17]. Figure 7d–f shows the morphology of $M_{23}C_6$ carbides in samples T460 and T580. It can be seen that quasi-spherical carbides are mainly observed at the boundary after being tempered at 460 °C, which are identified as $M_{23}C_6$ carbides

by the SAED pattern in Figure 7e, while thin-film carbides are observed in sample T580, which indicates that with the growth of $M_{23}C_6$ carbide, the discontinuous $M_{23}C_6$ particles precipitated at the boundary begin to connect to form film-shaped morphology. This phenomenon has also been reported in Ren's work [18].

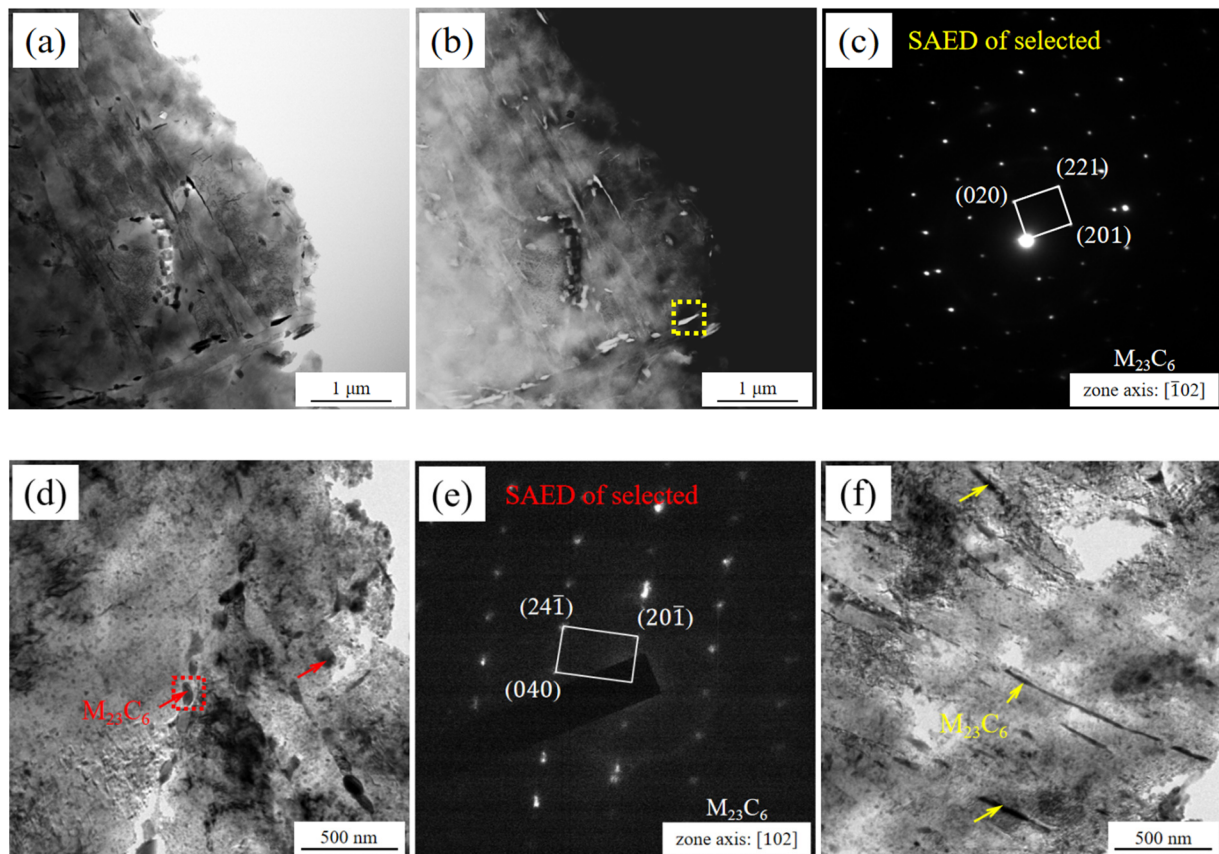


Figure 7. (a–c) STEM images of sample T500 and corresponding indexed precipitates SAED pattern. (d,e) Bright-field TEM micrographs and SAED pattern of $M_{23}C_6$ in sample T460. (f) Bright-field TEM micrographs of $M_{23}C_6$ in sample T580.

To accurately confirm the morphology and type of the fine nano-sized spherical particles precipitated in samples, EDS and high-resolution transmission electron microscopy (HRTEM) was conducted in combination, as presented in Figure 8. It can be seen from Figure 8a that a large amount of spherical-like nano-scale with a diameter of 5–15 nm is uniformly distributed on the martensite matrix of tempered sample. EDS analysis (Figure 8b) reveals that these fine particles or clusters are rich-Cu precipitates. When HRTEM under an incident beam aligned along the $[001]$ directions of the matrix is conducted, as shown in Figure 8c, it can be found that the observed interplanar spacing ($22\bar{2}$) for the rich-Cu precipitate is 0.108 nm. Fourier transform (FFT) patterns in the selected region are given in Figure 8d. The FFT pattern indicates that the rich-Cu phase structure is fcc structure, which is consistent with the previous results [19], and has the orientation relationship of $[011]_{Cu} // [001]_{\alpha}$ with the matrix. The lattice constants for rich-Cu precipitates are calculated as $a = b = c = 3.741 \text{ \AA}$, which is slightly greater than the lattice constants in fcc Cu (3.615 \AA). It may be caused by the other alloy elements with a larger atomic radius replacing the Cu atom, increasing the lattice constants of Cu precipitate. As shown in Figure 8e,f, the inverse FFTs (IFFTs) of selected \vec{g}_{222Cu} and $\vec{g}_{300\alpha'}$ spots are plotted. It can be seen that the interface is flat and coherent along the $[222]_{Cu}$ direction. However, there are a lot of edge misfit dislocations distributed mainly in the interface and aggregation region in IFFT images of yellow dotted box, which are observed along the $[300]_{\alpha'}$ direction, indicating

that the Cu interface shows semi-coherent with the matrix. The climbing and sliding of edge dislocations make the interface move toward the matrix along the $[010]_{\alpha'}$.

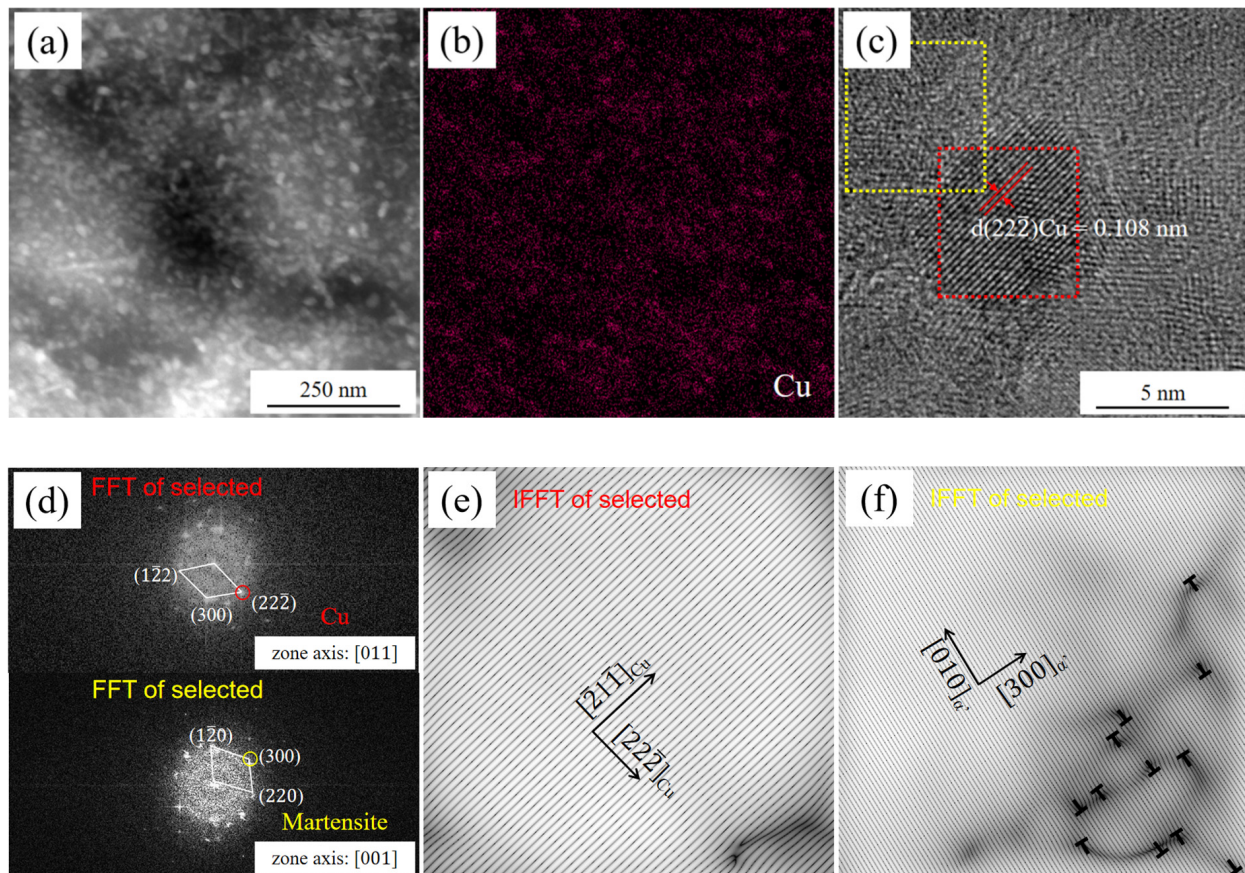


Figure 8. (a) TEM morphology of rich-Cu precipitates. (b) EDS element map corresponding to (a). (c) HRTEM image of spherical rich-Cu precipitates. (d) FFT patterns of selected regions in (c). (e,f) IFFT patterns of selected $\vec{g}_{222\text{Cu}}$ and $\vec{g}_{300\alpha'}$ spots.

Other spherical precipitates are observed in both steels, as shown in the red rectangles in Figure 9a. The dark field micrograph further shows their morphology, as shown in Figure 9b, presenting a relatively large number density. Diffraction patterns and EDS (inserted in Figure 9a,b) indicate there is only MC carbide. Because of its small size and the fact that it is easy to interact with defects such as dislocations, they are difficult to observe directly in TEM images. To further confirm the morphology and type, the carbon extraction replica method was applied, as shown in Figure 9c. Some particles larger than 40 nm in diameter can be directly observed and can be determined as MC carbides by SAED and dark field micrograph (Figure 9d–f). The illustration in Figure 9c shows the HRTEM image of MC particles. According to the distribution curves of the size of MC carbides, as shown in Figure 9g, it is found that the particles with a diameter less than 15 nm account for the main proportion. Figure 10a shows the evolution of equilibrium phases with temperature calculated using TC software (Version 2020a. Royal Institute of Technology (KTH), Stockholm, Sweden). It means NbC would still exist after quenching from 860 °C. Thus, the large NbC particles (>50 nm) observed after tempering may have been formed during austenitizing. The existence of these NbC particles can inhibit grain coarsening during austenitizing.

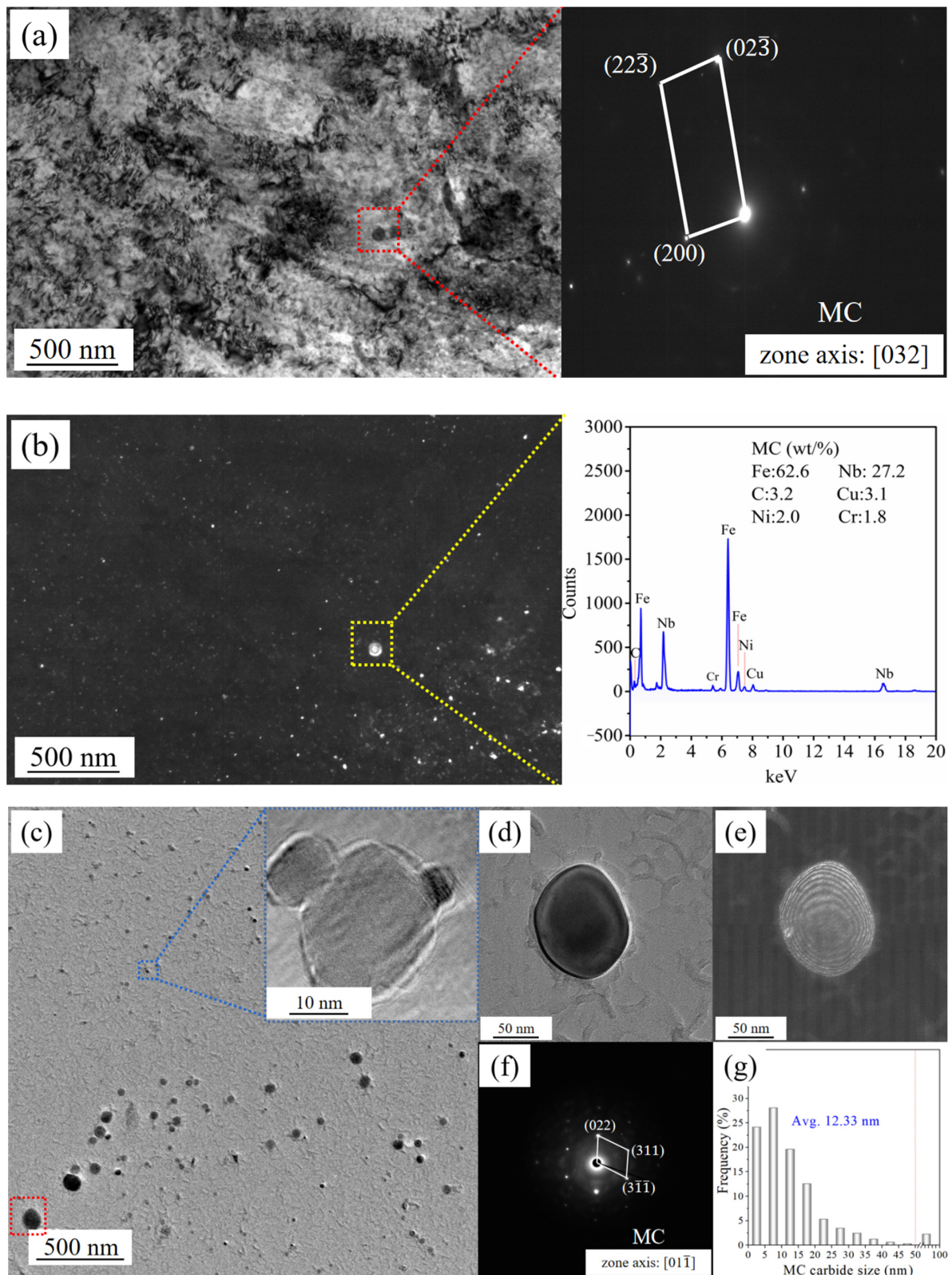


Figure 9. (a,b) TEM and dark field micrographs show the existence of nano-sized MC carbides after tempering. Inserted graphs in (a) and (b) show diffraction pattern and EDS spectrum of selected area, respectively. (c) TEM images of MC carbide prepared via the carbon extraction replica method. Inserted graph shows HRTEM image of selected area. (d–f) TEM, dark field micrographs and SAED pattern of MC carbide selected in the dotted box in (c). (g) The distribution curves of the size of MC carbides.

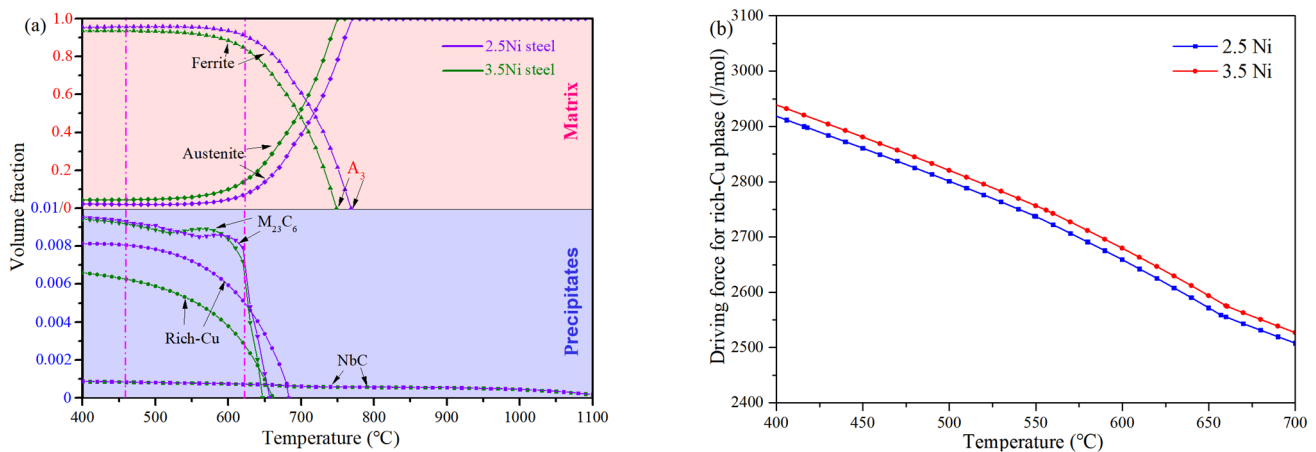


Figure 10. TC calculation results. (a) Volume fraction of equilibrium phases. (b) Driving force curves for rich-Cu precipitates.

In addition, a few coarse particles identified as Fe_3C are also observed in the TEM images of 3.5 Ni steel as shown in Figure 11. According to the calculation results of equilibrium phase, Fe_3C carbide will not precipitate at 860 °C. It can be concluded that the Fe_3C particles from the initial microstructure would be dissolved during the austenitizing treatment at 860 °C. As an austenite stabilized element, the increase of Ni content reduces the A_3 temperature (Figure 10a) and widens the austenite phase area. Thus, the dissolution kinetics of Fe_3C is accelerated at the same austenitizing temperature. Contrary to this general expectation, Park et al. found that the increase of Ni content decreased the dissolution of Fe_3C [14]. Apparently, the dissolution of Fe_3C at austenitizing temperature involves the diffusion of C atoms from Fe_3C to the adjacent matrix. Since the Fe_3C /matrix interface is surrounded by Ni-enriched austenite that has been transformed rapidly from ferrite, however, the diffusion of C is inhibited. It is then difficult for the complete dissolution of Fe_3C in 3.5 Ni steel. Furthermore, the $M_{23}C_6$ carbides are generally transformed from the nano-scale M_3C by the reaction ($M_3C \rightarrow M_7C_3 \rightarrow M_{23}C_6$) via in-situ transformation [20]. From this point of view, the residue of Fe_3C in 3.5 Ni steel will reduce the formation of $M_{23}C_6$ carbide.

Due to the strong correlation between crystallographic characteristics and mechanical properties, EBSD is used to analyze the crystallographic characteristics of the sample T500 with a large difference in cryogenic toughness between the two samples. The typical reconstructed grain boundary map and the grain misorientation angle distribution of both samples are shown in Figure 12a–c. The grain boundaries with misorientation angles of $2^\circ < \theta < 5^\circ$, $5^\circ < \theta < 15^\circ$ and $15^\circ < \theta$ are defined as low-angle grain boundaries (LAGBs), medium-angle grain boundaries (MAGBs) and HAGBs. The results indicate that the 3.5 Ni steels contain more HAGBs than 2.5 Ni steel. Figure 12d–f show the reconstructed maps and statistical results of coincidence site lattice (CSL) boundaries, respectively. Only $\Sigma 11$ CSL boundary exhibits a great difference between both samples. With increasing Ni content, $\Sigma 11$ boundary decreases significantly, and other CSL boundaries are almost unchanged.

In general, the microstructure evolution of both steels can be vividly represented by the schematic diagram, as shown in Figure 13. In the quenched state, the precipitation of NbC with high thermal stability on the grain boundary can inhibit the grain coarsening, but the increase of Ni makes the grain size of 3.5 Ni steel coarser than that of 2.5 Ni steel, and there remains a small amount of Fe_3C residue. During tempering, with the gradual merging of martensite laths, the dislocation density in tempered martensite decreases, and a large number of particles begin to precipitate and coarsen. Among them, the change of $M_{23}C_6$ carbide is the most obvious, and its shape gradually becomes thin film. In addition, with the increase of tempering temperature, austenite reverse transformation occurs, especially in 3.5 Ni. However, the diffusion of C at high temperature reduces the stability of austenite and makes it easy to be transformed into secondary martensite in the subsequent cooling,

which leads to a slight increase in dislocation density of steel. It is worth noting that during the coarsening and merging of martensite laths, various precipitates and reverse austenite still grow in their original positions and distribute on the tempered martensite matrix.

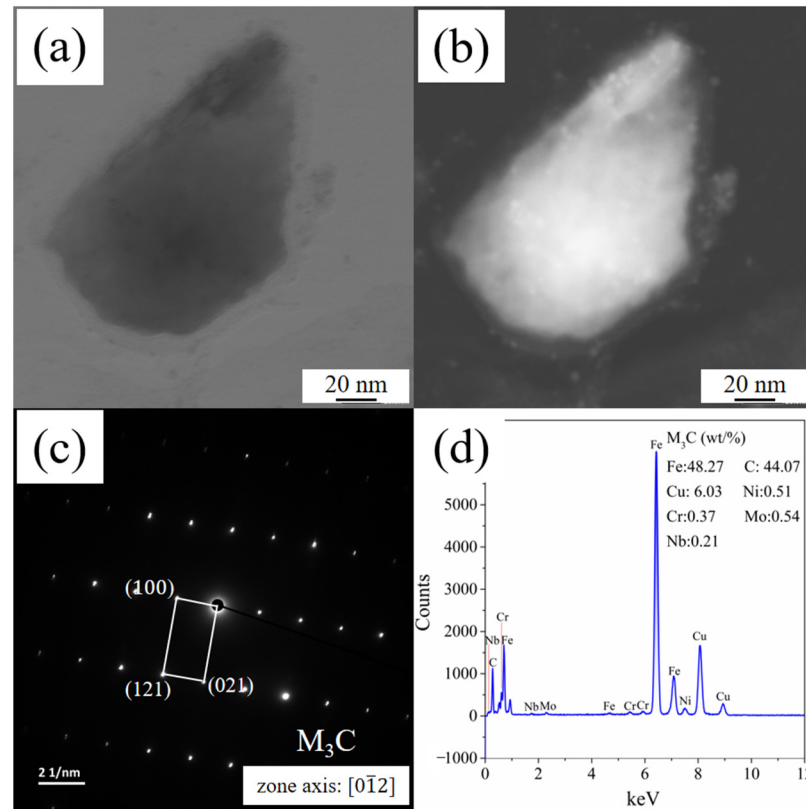


Figure 11. (a) TEM. (b) Dark field micrographs. (c) SAED patterns and (d) EDS of Fe_3C carbides in 3.5 Ni steel.

3.2. The Relationship between Microstructure and Mechanical Properties

The mechanical properties of investigated steels under different heat treatment conditions are presented in Figure 14. From Figure 14a, the yield strength and elongation of quenched 2.5 Ni steel is 1049 MPa and 14.4%, which are higher than that of 3.5 Ni steel. With increasing tempering temperature to 620 °C, the elongation of both steels increases and the yield strength decreases, except at 500 °C for 3.5 Ni steel. The yield strength of 3.5 Ni steel is 10–20 MPa larger than that of 2.5 Ni steel when tempered at 500 °C. Fracture surfaces of tensile tests are presented in Figure 15. Compared with 2.5 Ni steel, shallow and equiaxed dimples are observed in the fracture surface of 3.5 Ni steel after quenching at 860 °C. Due to the coarsening and gathering of dimples, small tear ridges appear as shown by the red arrow. After tempering at 460–620 °C, both steels show similar fracture surfaces. Taking the sample T500 of two steels as an example, the fracture morphology is shown in Figure 15c–f. As shown in Figure 15c,d, the low magnification fracture morphologies reveal the whole region of the fracture surface and show neck shrinkage after tensile deformation for both steels. The fracture surfaces are composed of fibrous region, radial region and shear lip region, and many delamination cracks (shown by white arrows) are observed in the radial region in a direction perpendicular to the primary crack plane. These delamination cracks should form during the post-necking regime of the tensile tests and attribute to plasticity [21]. Figure 15e,f present enlarged views of the selected region in Figure 15c,d. It can be found that both samples exhibit the ductile fracture mode comprising typical dimple morphologies.

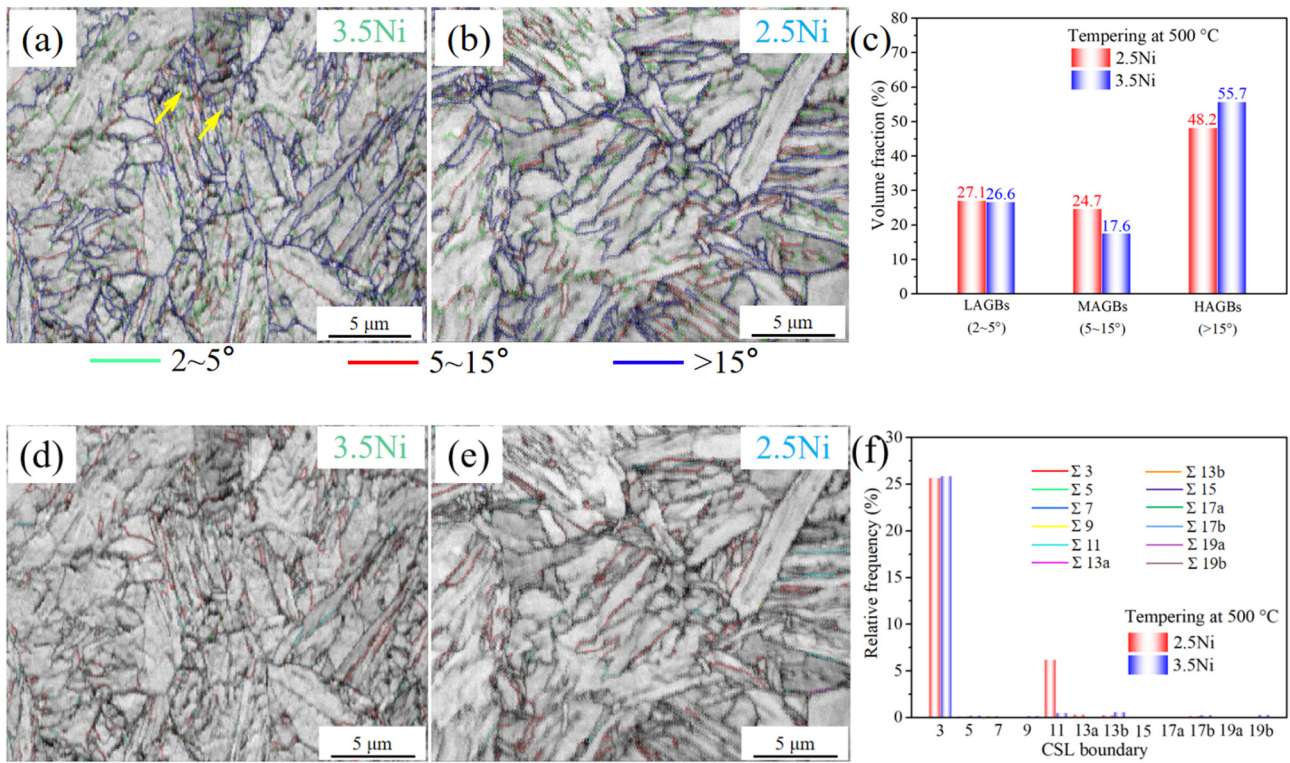


Figure 12. EBSD crystallographic analyses of both steels. (a,b) Misorientation distributions of grain boundaries. (c) Volume fraction of each grain boundary in the samples. (d,e) Reconstructed CSL boundary maps. (f) The frequency of each CSL boundary in the samples.

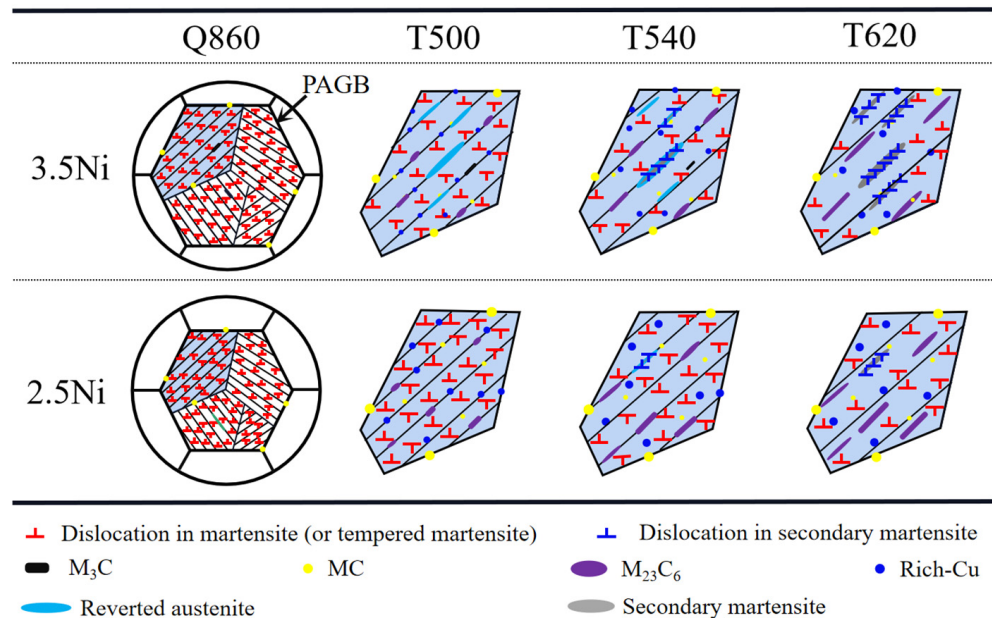


Figure 13. Schematic diagram of microstructure evolution of two steels after quenching and tempering at different temperatures.

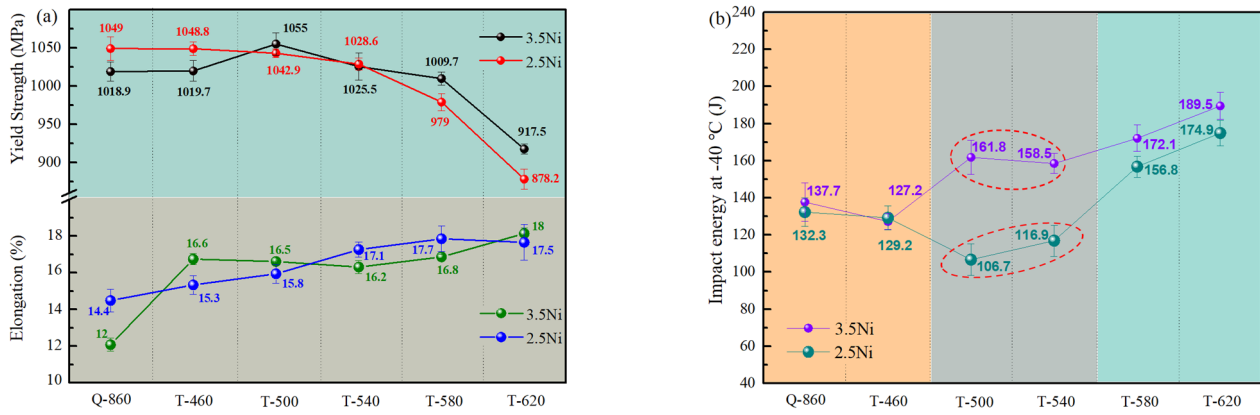


Figure 14. The mechanical properties of experimental steels. (a) Tensile properties at room temperature. (b) Cryogenic impact properties.

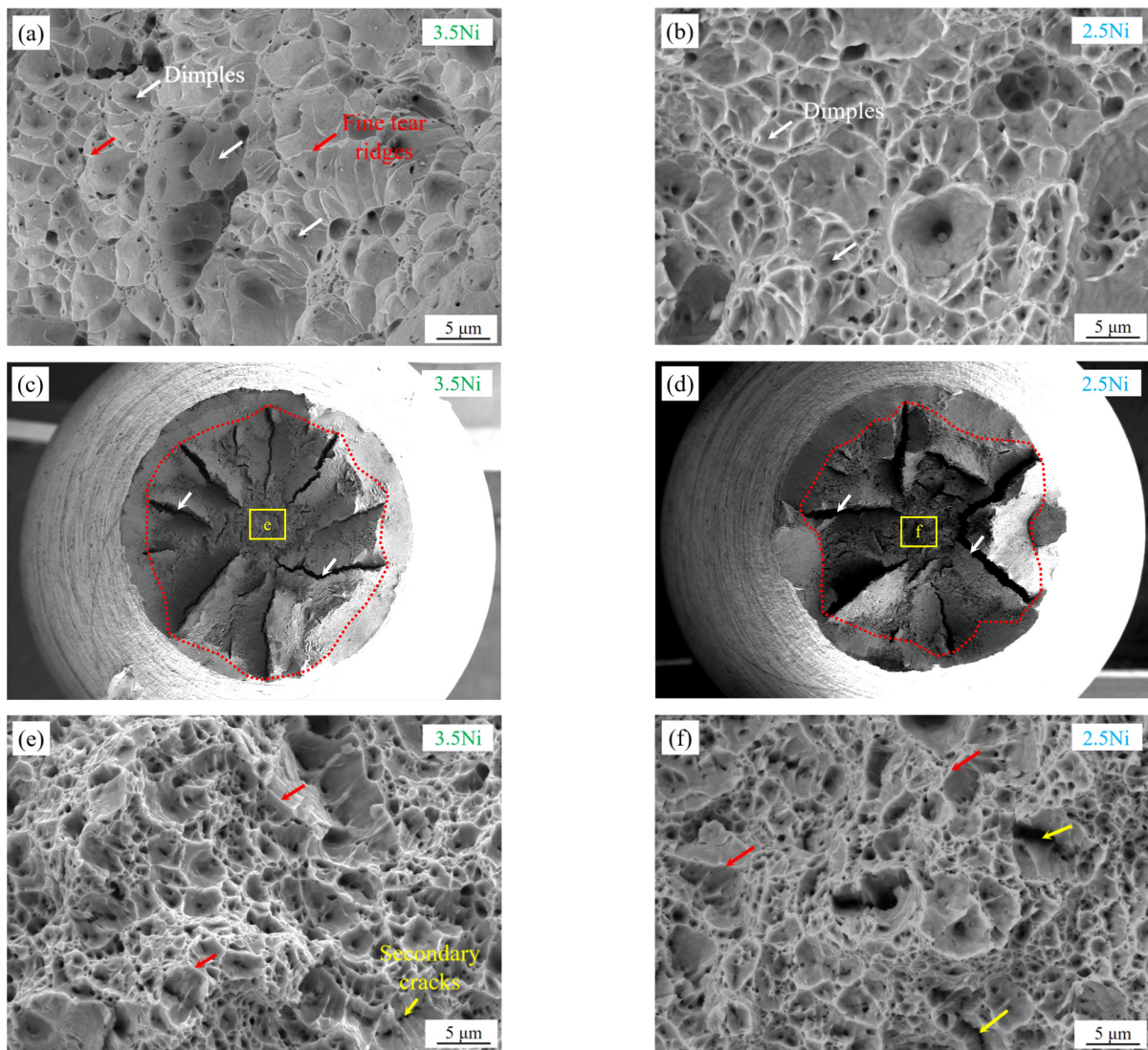


Figure 15. (a,b) Tensile fracture micrographs for the quenched samples. (c–f) Representative tensile fracture morphology of the two steels after tempering, taking samples T500 as an example; (c,d) The low magnification fracture morphologies of samples T500 of two steels; (e,f) showing high magnification image of region e and f in image (c,d).

Typically, the yield strength of the steel is correlated with the contributions of lattice friction stress of pure iron [22], solid solution strengthening [23], precipitation strengthening [22,24], grain boundary strengthening [25,26], and dislocation density strengthening at lath and sub-block boundaries [27]. Due to the fine grain strengthening effect of 2.5 Ni steel, its strength after quenching from 860 °C is greater than that of 3.5 Ni steel. Moreover, grain refinement also improves its plasticity. Because of the decomposition of martensite, the decrease in yield strength and increase in elongation are exhibited in the experimental steels with the increase of tempering temperature. It is noted that the yield strength of 3.5 Ni steel increases slightly after tempering at 500 °C. As mentioned above, the addition of Nb and Cu promotes the formation of NbC and rich-Cu nano-particles, which is the key factor for improving the yield strength. The precipitation strengthening effect of these particles in steels depends on the type, average size and volume fraction of precipitates, as well as their interactions with dislocations. As shown in Figure 10a, the increase in Ni content decreases the volume fraction of rich-Cu phase at the same Cu concentration. The volume fraction of Cu precipitation (f) is related to its radius (R) and particle number (N^*) according to the following equation [28]:

$$f = \frac{4\pi}{3} R^3 N^* \quad (3)$$

It is well-known that the maximum number of precipitates is directly proportional to the density of nucleation sites [29]. The number of nucleations is characterized by the nucleation rate, which can be expressed as shown in Equation (4) [30]:

$$N = \omega C_0 \cdot \exp\left(\frac{-\Delta G_m}{kT}\right) \cdot \exp\left(\frac{-16\pi\gamma^3}{3\Delta G_d^2 kT}\right) \quad (4)$$

where N is the nucleation rate, ω is a factor including the atomic vibration frequency and the critical nucleus area, C_0 is the concentration of the heterogeneous nucleation sites per unit volume, ΔG_m is the migration activation energy of a single atom, k is the Boltzmann constant, T is the temperature, γ is the surface free energy per unit area and ΔG_d is the nucleation driving force.

When tempered at a certain temperature, ω , C_0 , ΔG_m , k , T and γ are constant. Thus, the value of N depends on the ΔG_d . Figure 10b shows the driving force curves of the rich-Cu phase calculated by TC. The result shows that ΔG_d increases with increasing Ni content, indicating Ni can improve the number of rich-Cu precipitates. In addition, Seko et al. calculated the enthalpy change and interface energy using first principles, and revealed that the addition of Ni can increase the number density of rich-Cu precipitates by reducing the strain energy for nucleation and the interfacial energy between the matrix and the nuclei [31]. In this case, the number density of rich-Cu precipitates in 2.5 Ni steel is low, while the volume fraction is high, so the volume of a single particle is larger than that in 3.5 Ni steel. For MC carbides, under the same Nb content, the increase of Ni does not affect its volume fraction (Figure 10a). Moreover, the driving force of MC carbides of both steels tempered at 500 °C is 43,003.11 J/mol calculated by TC software. It can be inferred that the difference in Ni content will not cause the size and quantity of MC carbides in the two steels. Thus, the small increase of yield strength of 3.5 Ni steel is due to the precipitation of a large number of finer rich-Cu phases during tempering 500 °C.

As the temperature rises to 620 °C, the softening effect caused by martensite recovery is dominant and the precipitation strengthening effect is weakened due to the coarsening of rich-Cu particles. The yield strength of 3.5 Ni steel thus begins to decrease again. Compared with 2.5 Ni steel, the yield strength of 3.5 Ni steel is slightly higher due to the formation of secondary martensite.

Figure 14b shows that Ni affects the dependence of the impact toughness on the tempering temperature considerably. It can be seen that the cryogenic toughness of two steels presents different variations with tempering temperature. For sample Q860, the two steels have similar toughness. Compared with 2.5 Ni steel, the high dislocation density in 3.5 Ni steel makes up for the toughness loss caused by the coarser grain by delaying crack nucleation and relaxing the stress on the crack tip [32]. With the increase of tempering temperature, the impact energy of 3.5 Ni steel generally increases and the maximum impact energy can reach 189.5 J at 620 °C. In distinct contrast, the impact energy of 2.5 Ni steel drops slightly to 106 J when the tempering temperature increases to 500 °C, indicating the deterioration of toughness. Further increasing the tempering temperature can increase the impact energy of 2.5 Ni steel up to 174.9 J, which is close to that of 3.5 Ni steel.

As shown in Figure 7, a few quasi-spherical $M_{23}C_6$ carbides precipitated at the boundaries, then the cryogenic toughness of the two steels tempering at 460 °C decreased slightly because the interaction between dislocation and $M_{23}C_6$ carbide may lead to the formation of microvoids at the initial stage of fracture. With the tempering temperature increasing to 500–540 °C, $M_{23}C_6$ carbide gradually changes from quasi-spherical to short rod or even thin film, which will reduce the bonding force between grain boundaries and further deteriorate the toughness of steel. However, compared with 2.5 Ni steel, 3.5 Ni steel tempered at 500–540 °C not only has strong microstructure recovery, but also is accompanied by the precipitation of nano rich-Cu phase, which is conducive to the improvement of toughness. In addition, the grain boundary characteristics are characterized by EBSD to analyze the relationship between grain boundary and toughness. It can be seen that with the increase of Ni content, the proportion of LAGBs is not significantly changed, but the proportion of HAGBs is increased. Previous research indicated that LAGBs were able to enhance strength, while HAGBs could promote crack deflection during crack propagating and hinder the crack extension [26]. The HAGBs in lath martensite steel can separate the crystallization region, forming effective grains. According to the Griffith equation [33], cleavage fracture strength increases with effective grain refinement. This shows that the increase of Ni content can inhibit crack propagation by increasing the proportion of HAGBs and can improve the toughness of 3.5 Ni steel. Moreover, the relatively more austenite in sample T500 of 3.5 Ni steel is conducive to passivating the stress concentration at the crack tip and preventing crack propagation. Therefore, after tempering at 500–540 °C, 3.5 Ni steel not only has no toughness deterioration, and the impact energy is as high as 160 J. With an increase in tempering temperature up to 580 and 620 °C, impact toughness rapidly increased, which is ascribed to strong recovery and partial recrystallization (Figure 3c,f), especially for 3.5 Ni steel, the characteristics of martensitic lath almost disappear after tempering at 620 °C. In addition, as shown in the schematic diagram of sample T620 in Figure 13, during the coarsening and merging of martensitic laths, the $M_{23}C_6$ carbides distributed on the boundary are significantly reduced, which can reduce the adverse impact on toughness.

The marked differences can also be indicated by the fracture surfaces shown in Figure 16. The morphology of 3.5 Ni steel tempered at 500–540 °C is of a ductile character with dimples, while cleavage river patterns with a small quantity of dimples are observed in samples of 2.5 Ni steel, corresponding to their lower toughness, as shown in Figure 16d. Under other heat treatment processes, the two steels show a similar fracture mode, that is, sample Q860 and T460 are characterized by a cleavage river pattern and few shallow dimples, implying quasi-cleavage fracture, and various sizes of dimples were observed in the fracture surfaces of samples T580 and T620, exhibiting ductile fractures. The large dimples in samples T580 and T620 indicate that they undergo greater plastic deformation before failure [34].

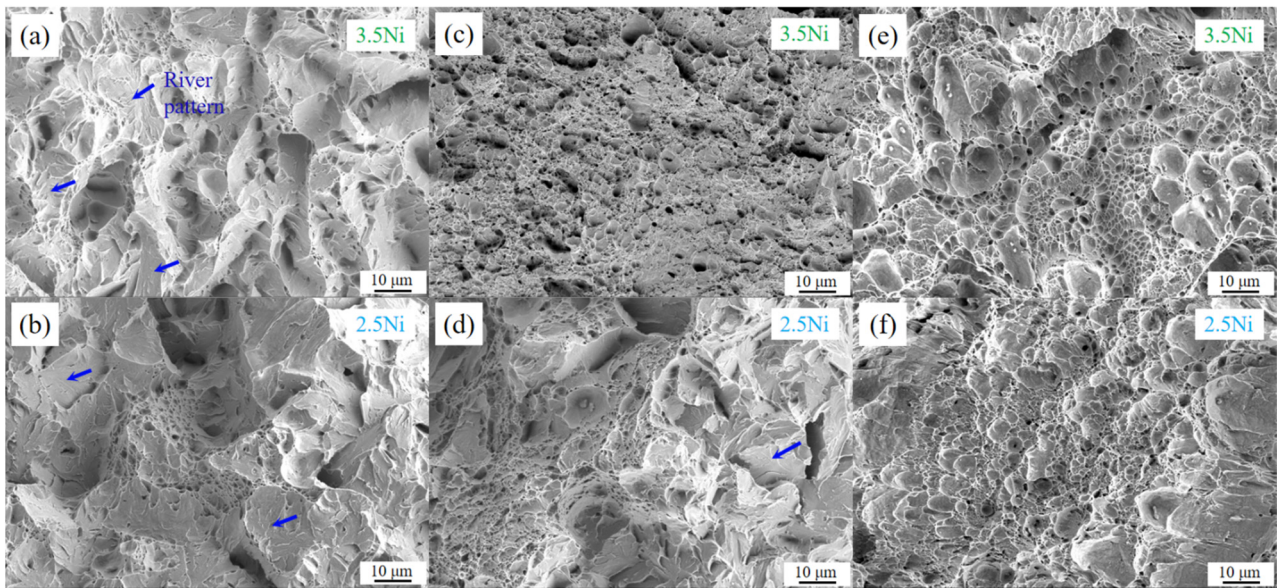


Figure 16. Representative impact fracture micrographs of two steels after different heat treatment processes. (a,b) Q860. (c,d) T500. (e,f) T620.

3.3. Hydrogen Embrittlement Susceptibility Analysis

Sample T500 of both steels were pre-charged with hydrogen to evaluate their hydrogen embrittlement resistance. The engineering stress-strain curves of sample T500 with or without hydrogen charging are presented in Figure 17a. In general, the total elongation and reduction of area deteriorate drastically, while the yield and tensile strength do not change notably on hydrogen charging. The comparison of results demonstrates that the hydrogen has different effects on the two samples. Figure 17b compares the elongation and reduction of area of the two steels before and after hydrogen charging, and shows the assessed hydrogen embrittlement susceptibility index. It can be seen that the two hydrogen embrittlement indexes of 2.5 Ni steel are both lower than those of 3.5 Ni steel, which indicates that the hydrogen embrittlement resistance of 2.5 Ni steel tempered at 500 °C is better than that of 3.5 Ni steel.

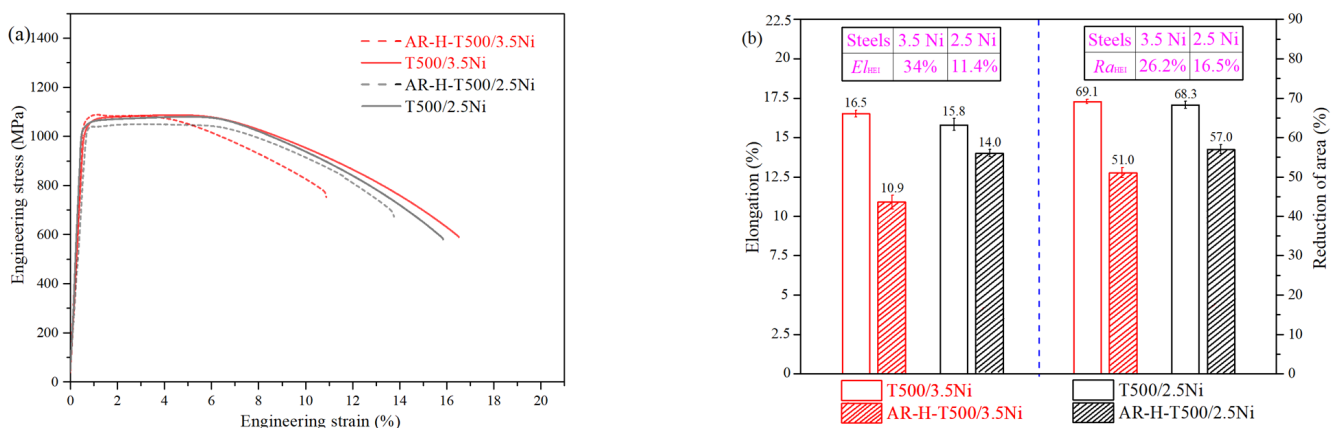


Figure 17. (a) Engineering stress-strain curves of hydrogen-free and hydrogen-charged samples. (b) Comparison of elongation and reduction of area of the two steels before and after hydrogen charging and the assessed hydrogen embrittlement susceptibility indexes.

It is known that the interaction of different microstructures with hydrogen atoms determines hydrogen uptake, diffusion, trapping, and effusion [35,36]. The microstructural characteristics, such as dislocations, grain boundaries, precipitates and inclusions, can act as different hydrogen traps to capture hydrogen atoms because they have different affinity with hydrogen atoms. TDS data is used to analyze the hydrogen trapping behavior of various microstructure characterization. As shown in Figure 18a, compared with 3.5 Ni steel, only one peak can be observed near 102 °C on the TDS curve of 2.5 Ni steel, which is usually caused by reversible hydrogen traps such as grain boundaries, dislocations and vacancies. The hydrogen desorbed at this peak is defined as diffusive hydrogen. Figure 18b shows the hydrogen content captured at this trap site, and it is found that the reversible hydrogen content of 2.5 Ni steel is 0.94 ppm, which is higher than 0.8 ppm of 3.5 Ni steel. Compared with the total hydrogen content in the specimens, almost all hydrogen in 2.5 Ni steel is reversible hydrogen, which shows that grain boundaries and dislocations are the main hydrogen capture positions of 2.5 Ni steel. According to the concept of hydrogen embrittlement proposed by Song and Curtin [37], hydrogen accumulation degree and the stress level around the crack tip are the main factors for hydrogen embrittlement. Based on microstructure characterization, it is easy to find that the dislocation density and total surface area of grain boundaries (including PAG grain boundaries and martensitic lath, packet and block grain boundaries) of the T500 sample of 2.5 Ni steel are higher than those of 3.5 Ni steel, which can provide more hydrogen traps to capture hydrogen. It is conducive to improving the hydrogen embrittlement resistance of 2.5 Ni steel. However, the higher dislocation density in the martensite makes hydrogen accumulation around the crack-tip easier and increases the hydrogen embrittlement susceptibility.

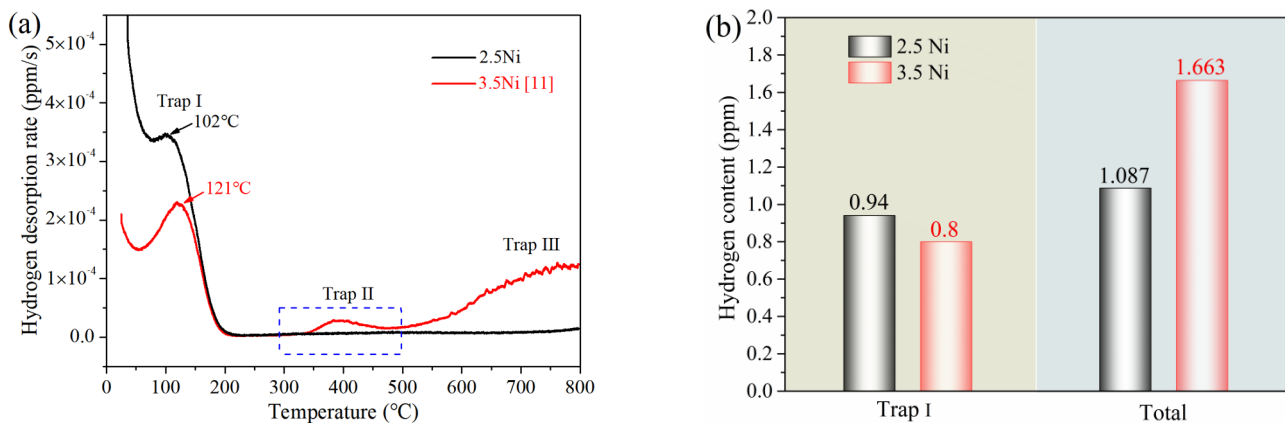


Figure 18. (a) Hydrogen desorption rate curves (TDS curves). (b) Hydrogen content of hydrogen-charged specimens.

According to previous studies [11], the peak observed at 340–395 °C on the TDS curve of 3.5 Ni steel is attributable to the hydrogen desorbed from nano-particles including NbC and rich-Cu precipitates. On the TDS curve of 2.5 Ni steel, no peak is directly observed in this temperature range, indicating that the hydrogen content captured by nano-particles is far lower than that of 3.5 Ni steel and not easy to detect. Compared with 3.5 Ni steel, 2.5 Ni steel has similar NbC particles, but the reduction of Ni reduces the nucleation energy of rich-Cu precipitates, thereby reducing the nucleation number of rich-Cu precipitates and increasing its particle size. Thus, the hydrogen trapping effect of rich-Cu particles should be weaker than that of 3.5 Ni steel [38]. In addition, the rich-Cu particles preferentially nucleated at grain boundaries and phase interfaces promote a transition from reversible to irreversible sites, which further reduces the diffusivity of hydrogen [39]. From this point of view, the hydrogen embrittlement resistance of 3.5 Ni steel should be better than that of 2.5 Ni steel, which is contrary to the evaluation results of hydrogen embrittlement

susceptibility. Therefore, it can be concluded that grain boundary is the key factor to improving the ability of capturing hydrogen atoms in 2.5 Ni steel.

The detailed grain boundary characteristics of both steels were examined by EBSD and were used to analyze their effect on hydrogen embrittlement. As shown in Figure 12, the increase in Ni content significantly increases HAGBs and slightly decreases LAGBs. In previous studies, LAGB was found to be beneficial against hydrogen-assisted cracking in bcc steels, while HAGB imposed the opposite effect [40]. In addition, CSL boundaries play an important role in trapping hydrogen in the material. It is well known that boundaries that have low Σ values are intensely resistant to boundary degradation such as intergranular corrosion, creep, and liquid metal embrittlement. In Figure 12f it can be seen that with the increase of Ni content, $\Sigma 3$ increases slightly and the $\Sigma 11$ decreases significantly. According to previous work, $\Sigma 3$ boundaries were not generated by twinning and could be considered HAGB, which increased the hydrogen embrittlement susceptibility in low carbon bcc steels [11]. In addition, the $\Sigma 11$ boundary was also reported to be crack resistance due to its lower misorientation angle and energy [41]. Based on the above results, the hydrogen assisted cracking resistance of 2.5 Ni steel is improved by reducing HAGBs fraction and increasing $\Sigma 11$ boundary.

In addition, another reason for improving the hydrogen embrittlement resistance of steel after reducing Ni content may be related to the residue of Fe_3C carbide [14]. According to Farelas's work, Fe_3C can act as a cathode with respect to the steel matrix and promote the preferential dissolution of the adjacent steel matrix [42]. The possible mechanism of hydrogen generation and absorption on the steel surface by neutral water corrosion is summarized simply by Equation (5) [14].



Part of the H^+ generated by the reaction overflows to the electrolyte and further reduces the pH value [43], and the other part accumulates in the corrosion pit near Fe_3C and then diffuses into the steel, which can increase the hydrogen embrittlement susceptibility of steel.

In Figure 19a,c, an overview of the fracture surfaces of both samples with hydrogen charging is presented. The neck shrinkage can still be observed after the tensile deformation of the hydrogen-charged sample of both steels. Compared to the hydrogen-free samples, the fracture surface morphologies of hydrogen-charged samples showed more shear lip region, which indicates that both steels have plastic deterioration. In addition, the radial region of 3.5 Ni steel decreases after hydrogen charging, and the delamination cracks perpendicular to the main crack surface largely disappear, while the change of this region of 2.5 Ni steel before and after hydrogen charging is not obvious, indicating that it still has good plasticity, which is consistent with the tensile test results. More detailed views of the central regions are shown in Figure 19b,d, respectively. It is shown in Figure 19d that a number of dimples occupy the majority of the region d, which indicates that the micro-void coalescence (MVC) is the main fracture mode in 2.5 Ni steel. Compared with 2.5 Ni steel, the fracture surface of 3.5 Ni steel shows an obvious tear ridge and secondary crack, exhibiting quasi-cleavage (QC) fracture mode. This is the result of localized plastic deformation. The appearance of tear ridge and secondary crack demonstrates that the hydrogen-enhanced localized plasticity (HELP) mechanism is the main mechanism of hydrogen embrittlement fracture in 3.5 Ni steel [11].

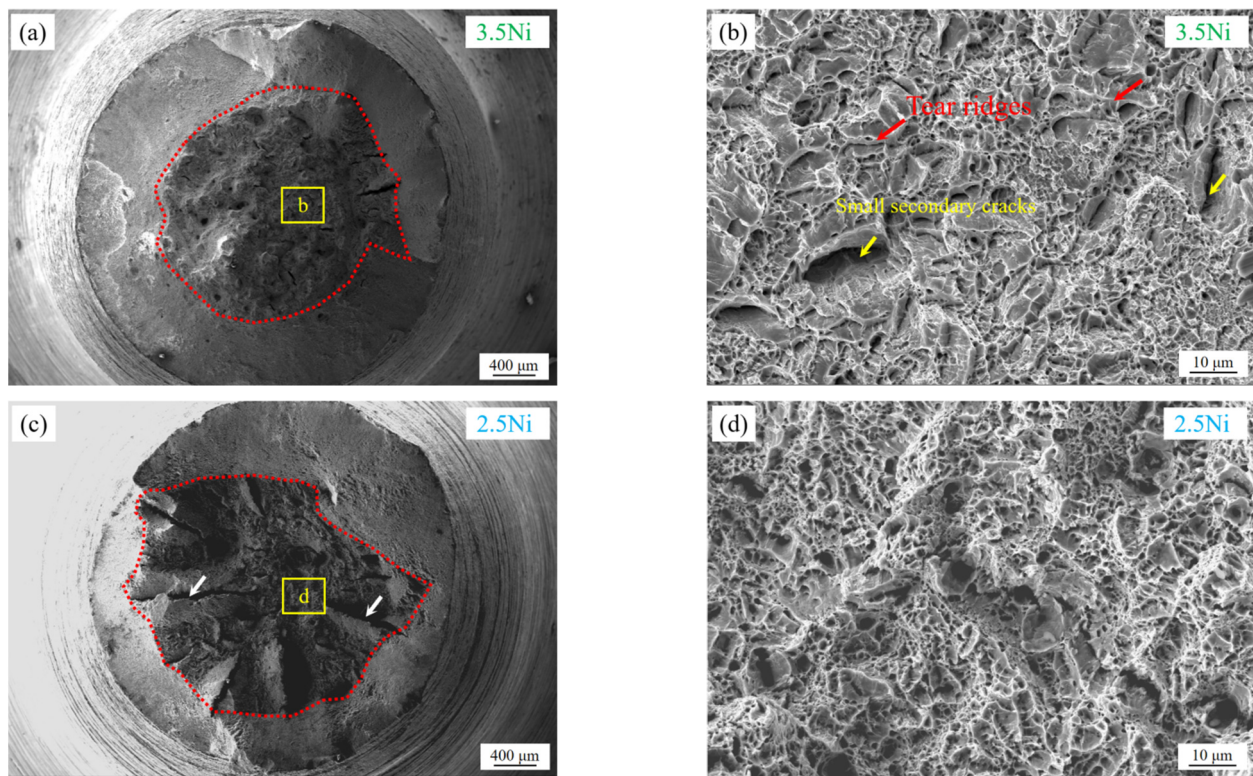


Figure 19. (a,c) SEM morphologies for the fracture surface in the hydrogen-charging specimens. (b,d) high magnification image of selected region.

4. Conclusions

Mechanical properties and microstructure evolution in two high-strength and high-toughness steels with different Ni content after tempering at different temperatures were investigated. The major findings are summarized as follows:

- (1) Because the reduction of Ni content increased the A_{C3} temperature of steel, the grain coarsening rate decreased at a given temperature, so the quenched 2.5 Ni steel had high strength and plasticity. With tempering temperature increasing from 460 °C to 620 °C, the yield strength of 2.5 Ni steel decreased continuously, while 3.5 Ni steel attained its maximum yield strength value of 1055 MPa tempered at 500 °C. Combined with the thermodynamic analysis, Ni content affected the volume fraction and nucleation number of rich-Cu precipitates, resulting in different precipitation strengthening effects in the two steels.
- (2) There were obvious differences in cryogenic impact toughness and fracture mode between the two steels, especially after tempering at 500–540 °C. Besides the strong precipitation of the rich-Cu phase and improved microstructure recovery, the increase of Ni content accelerated the reverse transformation of austenite according to thermodynamic and kinetic analyses. In addition, comparing the grain boundary characteristics of the two steels after tempering at 500 °C, it was found that the increase of Ni content led to the increase of HAGBs proportion, which could inhibit crack propagation and increase cleavage fracture strength.
- (3) The hydrogen embrittlement susceptibility of the two steels after tempering at 500 °C was evaluated by comparing the tensile properties before and after hydrogen charging. The results showed that the reduction of Ni content improved the hydrogen embrittlement resistance of steel. Combined with microstructure characteristics and TDS analysis, it was found that 2.5 Ni steel with higher hydrogen brittleness resistance benefitted from the increase in grain boundary density in steel due to grain refinement. Moreover, with the decrease in Ni content, the decrease of HAGBs and the increase in

$\Sigma 11$ boundary were conducive to reducing hydrogen assisted cracking. In addition, the residual Fe_3C in steel would deteriorate the hydrogen embrittlement resistance of steel.

Author Contributions: N.Z.: Methodology, Software, Investigation, Writing-original draft. Y.H.: Writing-review and editing. L.L.: Supervision. R.L.: Supervision. Q.Z.: Experiment and data acquisition. W.Z.: Software. All authors have read and agreed to the published version of the manuscript.

Funding: This research was funded by [National Natural Science Foundation of China] grant number [51971127] and the APC was funded by [National Natural Science Foundation of China].

Institutional Review Board Statement: Not applicable.

Informed Consent Statement: Not applicable.

Data Availability Statement: Not applicable.

Conflicts of Interest: We declare that we have no known competing financial and personal relationships with other people or organizations that can inappropriately influence our work. There is no professional or other personal interest of any nature or kind in any product, service and/or company that could be construed as influencing the position presented in, or the review of, the manuscript entitled: “Strength-toughness balance and hydrogen embrittlement susceptibility of a precipitation-strengthened steel adopted tempering process”.

References

1. Xi, X.H.; Wang, J.L.; Chen, L.Q.; Wang, Z.D. Understanding the role of copper addition in low-temperature toughness of low-carbon, high-strength steel. *Met. Mater. Trans. A* **2019**, *50*, 5627–5639. [[CrossRef](#)]
2. Imai, N.; Komatsubara, N.; Kunishige, K. Effect of Cu and Ni on Hot Workability of Hot-rolled Mild Steel. *ISIJ Int.* **2007**, *37*, 224–231. [[CrossRef](#)]
3. Zhang, W.X.; Chen, Y.Z.; Cong, Y.B.; Liu, Y.H.; Liu, F. On the austenite stability of cryogenic Ni steels: Microstructural effects: A review. *J. Mater. Sci.* **2021**, *56*, 12539–12558. [[CrossRef](#)]
4. Nakada, N.; Syarif, J.; Tsuchiyama, T.; Takaki, S. Improvement of strength-ductility balance by copper addition in 9% Ni steels. *Mater. Sci. Eng. A* **2004**, *374*, 137–144. [[CrossRef](#)]
5. Hou, W.; Liu, Q.D.; Gua, J.F. Nano-sized austenite and Cu precipitates formed by using intercritical tempering plus tempering and their effect on the mechanical property in a low carbon Cu bearing 7 Ni steel. *Mater. Sci. Eng. A* **2020**, *780*, 139186. [[CrossRef](#)]
6. Cao, H.W.; Luo, X.H.; Zhan, G.F.; Liu, S. Effect of Intercritical Quenching on the Microstructure and Cryogenic Mechanical Properties of a 7 Pct Ni Steel. *Met. Mater. Trans. A* **2017**, *48*, 4403–4410. [[CrossRef](#)]
7. Chen, Q.Y.; Zhang, W.N.; Xie, Z.L.; Ren, J.K.; Chen, J.; Liu, Z.Y. Influence of intercritical temperature on the microstructure and mechanical properties of 6.5 Pct Ni steel processed by ultra-fast cooling, intercritical quenching and tempering. *Met. Mater. Trans. A* **2020**, *51*, 3030–3041. [[CrossRef](#)]
8. Zhao, N.; Zhao, Q.Q.; He, Y.L.; Liu, R.D.; Liu, W.Y.; Zheng, W.S.; Lin, L.I. Strengthening-toughening mechanism of cost-saving marine steel plate with 1000 MPa yield strength. *Mater. Sci. Eng. A* **2022**, *831*, 142280. [[CrossRef](#)]
9. Khare, A.; Vishwakarma, M.; Parashar, V. A review on failures of industrial components due to hydrogen embrittlement and techniques for damage prevention. *Int. J. App. Eng. Res.* **2017**, *12*, 1784–1792.
10. Ohaeri, E.; Szpunar, J.; Fazeli, F.; Arafin, M. Hydrogen induced cracking susceptibility of API 5L X70 pipeline steel in relation to microstructure and crystallographic texture developed after different thermomechanical treatments. *Mater. Charact.* **2018**, *145*, 142–156. [[CrossRef](#)]
11. Zhao, N.; Zhao, Q.Q.; He, Y.L.; Liu, R.D.; Zheng, W.S.; Liu, W.Y.; Zhang, Y. Investigation on hydrogen embrittlement susceptibility in martensitic steels with 1000 MPa yield strength. *J. Mater. Res. Technol.* **2021**, *15*, 6883–6900. [[CrossRef](#)]
12. Cunha, R.P.C.; Barbosa, C.; Barrozo, R.F.; CVelascoc, J.A.; Tavares, S.S.M. Influence of heat treatments on the susceptibility of 9%Ni low carbon steel to sulfide stress corrosion cracking. *Eng. Fail. Anal.* **2020**, *113*, 104554. [[CrossRef](#)]
13. Hui, W.J.; Zhang, H.X.; Zhang, Y.J.; Zhao, Z.L.; Shao, C.W. Effect of Nickel on hydrogen embrittlement behavior of medium-carbon high strength steels. *Mater. Sci. Eng. A* **2016**, *674*, 615–625. [[CrossRef](#)]
14. Park, J.S.; Seong, H.G.; Hwang, J.; Kim, S.J. Adverse effects of Ni on the mechanical and corrosion-induced hydrogen embrittlement properties of ultra-strong giga steel used for automotive applications. *Mater. Des.* **2020**, *193*, 108877. [[CrossRef](#)]
15. HajyAkbar, F.; Sitetsma, J.; Böttger, A.J.; Santofimia, M.J. An improved X-ray diffraction analysis method to characterize dislocation density in lath martensitic structures. *Mater. Sci. Eng. A* **2015**, *639*, 208–218. [[CrossRef](#)]
16. Zhao, Y.; Tong, X.; Wei, X.H.; Xu, S.S.; Lan, S.; Wang, X.L.; Zhang, Z.W. Effects of microstructure on crack resistance and low-temperature toughness of ultra-low carbon high strength steel. *Int. J. Plast.* **2019**, *116*, 203–215. [[CrossRef](#)]
17. Saha, D.C.; Biro, E.; Gerlich, A.P.; Zhou, Y. Effects of tempering mode on the structural changes of martensite. *Mater. Sci. Eng. A* **2016**, *673*, 467–475. [[CrossRef](#)]

18. Ren, W.H.; Wang, L.M. Precipitation behavior of M23C6 in high Nitrogen austenitic heat-resistant steel. *J. Alloys Compd.* **2022**, *905*, 164031. [[CrossRef](#)]
19. Li, Z.T.; Chai, F.; Yang, C.F.; Yang, L. Co-precipitation mechanism of nanoscale particles and mechanical properties in multicomponent ultra-high strength low carbon steel. *Mater. Sci. Eng. A* **2019**, *748*, 128–136. [[CrossRef](#)]
20. Pickering, F.B. The Precipitation of Cr₇C₃ in Ferritic Steels of Varying Chromium Content. In *Physikalisch-Technischer Teil*; Springer: Berlin/Heidelberg, Germany, 1960; pp. 668–670.
21. Pineau, A.; Benzerga, A.A.; Pardoën, T. Failure of metals I: Brittle and ductile fracture. *Acta Mater.* **2016**, *107*, 424–483. [[CrossRef](#)]
22. Chen, W.J.; Gao, P.F.; Wang, S.; Zhao, X.L.; Zhao, Z.Z. Strengthening mechanisms of Nb and V microalloying high strength hot-stamped steel. *Mater. Sci. Eng. A* **2020**, *797*, 140115. [[CrossRef](#)]
23. Yong, Q.L. *Secondary Phase in the Steel*; Metallurgical Industry Press: Beijing, China, 2006.
24. Gladman, T. Precipitation hardening in metals. *Mater. Sci. Technol.* **1999**, *15*, 30–36.
25. Kim, B.; Boucard, E.; Sourmail, T.; Martin, D.S.; Gey, N.; Rivera-Díaz-del-Castillo, P.E.J. The influence of silicon in tempered martensite: Understanding the microstructure-properties relationship in 0.5–0.6wt.%C steels. *Acta Mater.* **2014**, *68*, 169–178. [[CrossRef](#)]
26. Hansen, N. Hall-Petch relation and boundary strengthening. *Scr. Mater.* **2004**, *51*, 801–806. [[CrossRef](#)]
27. Hu, B.; He, B.; Cheng, G.; Yen, H.; Huang, M.; Luo, H. Super-high-strength and formable medium Mn steel manufactured by warm rolling process. *Acta Mater.* **2019**, *174*, 131–141. [[CrossRef](#)]
28. Tian, C.; Guo, H.; Hu, B.; Enomoto, M.; Shang, C.J. Influence of nano-scale concentration gradient of alloying elements on the ductility in an intercritically annealed and tempered medium Mn steel. *Mater. Sci. Eng. A* **2021**, *810*, 141009. [[CrossRef](#)]
29. Perrard, F.; Deschamps, A.; Maugis, P. Modelling the precipitation of NbC on dislocations in α -Fe. *Acta Mater.* **2007**, *55*, 1255–1266. [[CrossRef](#)]
30. Porter, D.A.; Easterling, K.E.; Sherif, M.Y. *Phase Transformation in Metals and Alloys*; CRC Press: Beijing, China, 2011.
31. Seko, A.; Odagaki, N.; Nishitani, S.R.; Tanaka, I.; Adachi, H. Free-Energy Calculation of Precipitate Nucleation in an Fe-Cu-Ni Alloy. *Mater. Trans.* **2004**, *45*, 1978–1981. [[CrossRef](#)]
32. Zhao, Y.J.; Ren, X.P.; Hu, Z.L.; Xiong, Z.P.; Zeng, J.M.; Hou, B.Y. Effect of tempering on microstructure and mechanical properties of 3Mn-SiNi martensitic steel. *Mater. Sci. Eng. A* **2018**, *711*, 397–404. [[CrossRef](#)]
33. Naylor, J.; Blondeau, R. The respective roles of the packet size and the lath width on toughness. *Met. Mater. Trans. A* **1976**, *7*, 891–894. [[CrossRef](#)]
34. Yan, P.; Liu, Z.; Bao, H.; Weng, Y.Q.; Liu, W. Effect of tempering temperature on the toughness of 9Cr-3W-3Co martensitic heat resistant steel. *Mater. Des.* **2014**, *54*, 874–879. [[CrossRef](#)]
35. Fuchigami, H.; Minami, H.; Nagumo, M. Effect of grain size on the susceptibility of martensitic steel to hydrogen-related failure. *Philos. Mag. Lett.* **2006**, *86*, 21–29. [[CrossRef](#)]
36. Tsay, L.W.; Chi, M.Y.; Wu, Y.F.; Wu, J.K.; Lin, D.Y. Hydrogen embrittlement susceptibility and permeability of two ultra-high strength steel. *Corros. Sci.* **2006**, *48*, 1926–1938. [[CrossRef](#)]
37. Song, J.; Curtin, W.A. Atomic mechanism and prediction of hydrogen embrittlement in iron. *Nat. Mater.* **2013**, *12*, 145–151. [[CrossRef](#)] [[PubMed](#)]
38. Song, H.; Jo, M.; Kim, D.W. Vanadium or copper alloyed duplex lightweight steel with enhanced hydrogen embrittlement resistance at room temperature. *Mater. Sci. Eng. A* **2021**, *817*, 141347. [[CrossRef](#)]
39. Yoo, J.; Jo, M.C.; Kim, D.W.; Song, H.; Koo, M.; Sohn, S.S.; Lee, S. Effects of Cu addition on resistance to hydrogen embrittlement in 1 GPa-grade duplex lightweight steels. *Acta Mater.* **2020**, *196*, 370–383. [[CrossRef](#)]
40. Zhang, S.; Fan, E.; Wan, J.; Liu, J.; Huang, Y.; Li, X. Effect of Nb on the hydrogen-induced cracking of high-strength low-alloy steel. *Corros. Sci.* **2018**, *139*, 83–96. [[CrossRef](#)]
41. Arafin, M.A.; Szpunar, J.A. A new understanding of intergranular stress corrosion cracking resistance of pipeline steel through grain boundary character and crystallographic texture studies. *Corros. Sci.* **2009**, *51*, 119–128. [[CrossRef](#)]
42. Farelas, F.; Galicia, M.; Brown, B.; Nesis, S.; Castaneda, H. Evolution of dissolution processes at the interface of carbon steel corroding in a CO₂ environment studied by EIS. *Corros. Sci.* **2010**, *52*, 509–517. [[CrossRef](#)]
43. Tsuru, T.; Huang, Y.L.; Ali, M.R.; Nishikata, A. Hydrogen entry into steel during atmospheric corrosion process. *Corros. Sci.* **2005**, *47*, 2431–2440. [[CrossRef](#)]